Solid State Communications 175-176 (2013) 18–34

Contents lists available at ScienceDirect

Solid State Communications

journal homepage: www.elsevier.com/locate/ssc

Gate modulated Raman spectroscopy of graphene and carbon nanotubes

R. Saito [a,*], K. Sato [a], P.T. Araujo [b], D.L. Mafra [b], M.S. Dresselhaus [b,c]

[a] Department of Physics, Tohoku University, Sendai 980-8578, Japan
[b] Department of Electrical Engineering and Computer Science, Massachusetts Institute of Technology, Cambridge, MA 02139, USA
[c] Department of Physics, Massachusetts Institute of Technology, Cambridge, MA 02139, USA

ARTICLE INFO

Article history:
Received 11 February 2013
Received in revised form
4 May 2013
Accepted 14 May 2013
Accepted by A. Lichtenstein
Available online 23 May 2013

Keywords:
A. Graphene
A. Carbon nanotubes
D. Double resonance Raman spectra
E. Gate modulated Raman spectroscopy

ABSTRACT

Gate-modulated Raman spectroscopy is a method of making Raman measurements while changing the Fermi energy by applying a gate voltage to the sample. In this review article, we overview the techniques of gate modulated Raman spectroscopy in graphene and carbon nanotubes (1) for assigning the combination phonon modes, (2) for understanding the optical processes involved in Raman spectra, and (3) for understanding the electron–phonon interaction not only for zone-center ($q=0$) phonons but also for double resonance phonons ($q\neq0$). The gate modulated Raman spectra are used in carbon nanotubes, too, especially for understanding electron–electron interaction from the electronic Raman spectra that are observed in metallic carbon nanotubes. Finally we discuss our recent work on gate-modulated Raman spectroscopy on bilayer graphene in which we explain how to get information about the interlayer interactions from gate modulated Raman spectroscopy.

1. Introduction

Raman scattering is the inelastic scattering of light in a solid (or a molecule) in which the energy shifts (or Raman shifts) from the incident light are frequently measured in units of cm^{-1} (1 eV = 8065 cm^{-1}) [1,2]. Raman spectroscopy has been widely used in nano-carbon materials, such as graphene and single wall carbon nanotubes (SWNTs) mainly for sample characterization, such as for defect states in graphene samples [3] or for the diameter distribution of SWNTs [4]. When we observe the Raman spectra by changing the energy of the incident light, the Raman intensity is enhanced when the incident or scattered light has the same energy as the optical transition energy of the solid, which is called *resonance Raman spectroscopy*. From resonance Raman spectroscopy, we can get information about the electronic structure of the solid which is especially significant in low-dimensional materials such as SWNTs or graphene because the density of states becomes singular and these characteristic effects are known as the van Hove singularity and exciton effects [5].

The energy loss (or gain) of the incident light in the inelastic scattering process is due to generating (or annihilating) elementary excitations, such as phonons or an electron–hole pair. The elementary excitations are coupled to photo-excited carriers as far as the corresponding interactions exist. For example, a phonon can couple with a photo-excited electron by an electron–phonon (or exciton–phonon) interaction. The generation of an electron–hole pair in the metallic energy bands of metallic nanotubes (m-SWNTs) or graphene can couple with photo-excited electrons (or excitons) by the electron–electron interaction. Further, a phonon directly generating an electron–hole pair is known as an infrared absorption of the phonon, and a photon is directly coupled with an atomic vibration by an electric-dipole interaction. Thus, we have many possible optical processes for photo-excited carriers in the inelastic scattering of light and we must investigate what kind of optical processes are dominant in the observed Raman spectra by changing parameters such as the incident laser energy (the resonance Raman effect), pressure, temperature, and the Fermi energy.

When the observed Raman spectra occur by phonon generating processes, we can check the phonon emitting process by observing the change of the Raman shifts when we substitute ^{12}C for ^{13}C (the isotope effect, see for example Ref. [6]). When the observed Raman spectra occur by generating an electron–hole pair, we can examine this process by observing the change in the Raman spectra resulting from changing the Fermi energy (gate modulated Raman effect). By increasing (or decreasing) the Fermi energy, the electron–hole pair generation can be suppressed because the final state (the initial state) becomes occupied (unoccupied). Even though we understand by gate modulated Raman spectroscopy that the Raman spectra are due to electron–hole pair generation, we do not know what kind of interaction is dominant for

* Corresponding author. Tel.: +81 22 795 7754; fax: +81 22 795 6447.
E-mail address: rsaito@flex.phys.tohoku.ac.jp (R. Saito).

0038-1098/$ - see front matter © 2013 Elsevier Ltd. All rights reserved.
http://dx.doi.org/10.1016/j.ssc.2013.05.010

generating an electron–hole pair, since there are two possibilities for the interaction. One is the electron–electron interaction and another is the electron–phonon interaction, as is discussed below. Thus by combining experiment with theory, we need to analyze the measured spectra in detail to answer this question.

For the case of metallic SWNTs or monolayer graphene, the phonon energy in the presence of the electron–phonon interaction is calculated using a perturbation Hamiltonian, in which the phonon frequency and phonon life time are "renormalized" in the sense that the phonon energy in a solid is originally normalized by the electron–phonon interaction which is based on discussions by Bardeen and Pine in the 1950s. The phonon softening phenomena by which an electron–hole pair is virtually excited in the perturbation expansion by the electron–phonon interaction is generally called "the Kohn anomaly effect" [7,8]. The Kohn anomaly effect is a non-adiabatic phenomena in the sense that the electron system can not remain in the ground state and the electron system always is shaken up by an atomic vibration. In a system for which an adiabatic approximation works, on the other hand, the electrons quickly follow the atomic vibration while keeping their electronic ground state. In a non-adiabatic system, the electrons can not relax quickly to their ground states, since a typical time for the relevant electron–phonon interaction (100 fs) is comparable or longer than the period of the lattice vibration (10–100 fs). Such a situation for the electrons can be imagined by considering water in a vibrating cup. The Kohn anomaly effect can be suppressed by changing the Fermi energy, and the effect can be probed by gate modulated Raman spectroscopy. Here we discuss how the Raman spectra is modified by changing the Fermi energy and what unique information we can get from such a gate-modulated Raman spectroscopy study.

Another interaction which can generate an electron–hole pair in the metallic energy band is the electron–electron interaction for photo-excited carriers or excitons in SWNTs. A part of the energy of the exciton can be transferred to generate another exciton in the metallic energy band in SWNTs by an electron–electron interaction. The inelastic scattering of the exciton which can be observed by a Raman spectroscopy approach is called *electronic Raman spectroscopy* (*ERS*). Similar to the Kohn anomaly, the ERS process can be suppressed by changing the Fermi energy, so that the ERS process can also be probed by gated modulated spectroscopy.

Finally we briefly explain: (1) first order and second order Raman scattering as well as (2) the intravalley and intervalley scattering of excitons in SWNTs or of an electron–hole pair in graphene [1].

In Raman spectroscopy, we have several characteristic features in the Raman spectra associated with different phonon modes and we also have ERS. Each optical process is either a first-order or a second-order Raman scattering process. In first-order Stokes (or anti-Stokes) Raman scattering, a Raman active phonon is emitted (or absorbed). If the phonon has a wavevector $-q$, a photo-excited electron at a state with wavevector k is scattered to a state with wavevector $k+q$. In order for the scattered electron to recombine with a hole having the same wavevector k, the phonon wavevector of the first-order scattering should be $q=0$, which we call the zone-center phonon mode. Even though we have a phonon dispersion relation with many q's, we only see the zone-center phonon at the Γ point in the reciprocal lattice (or Brillouin zone) in the first-order Raman process. In second-order scattering processes, on the other hand, two phonons can be emitted in an optical process induced by a photo-excited electron. In this case, an electron–hole pair of q and $-q$ with a $q\neq0$ phonon can be emitted in a two-phonon Raman process. If the two phonons are in the same phonon dispersion curve, the Raman spectrum is an overtone mode with twice the energy of the phonon, while in other cases, the Raman spectrum consists of a combination mode with the sum of the energies of the two phonons. In the second-order Raman spectra, since the limitation of $q=0$ in the first-order Raman spectra is relaxed and since there are many combinations of phonon modes, the assignment of the combination modes for a given Raman spectra is not easy especially for cases when the energies of two combination modes are close to each other. Here we give an overview showing how gate-modulated Raman spectroscopy can assign the combination modes even though the Raman features are close in frequency or the features are almost overlapped in frequency.

In Section 2, we introduce the experimental technique of the gate modulated Raman spectroscopy. In Section 3, we discuss the Kohn anomaly theoretically. In Section 4 we overview the main results of the gate-modulated Raman spectra and its analysis by theoretical considerations. In Section 5, electronic Raman spectra are overviewed, and in Section 6, Raman results for the in-plane and interlayer modes in bilayer graphene are given. In Section 7, a summary and future directions for the gate-modulation technique are given.

2. Gate modulated devices

Here we explain how to change the Fermi energy in the experiment by back gated and top gated devices. Two experimental techniques are employed: (1) back gated devices on a p-type silicon substrate and (2) top gated devices used with electro-chemical doping. In the back gated devices, as shown in Fig. 1(a), an applied gate voltage V_g can induce a potential difference between the silicon substrate and the graphene with a metallic contact separated by a silicon oxide (SiO_2, insulator) layer. When the V_g is positive or negative relative to the Si substrate, electrons or holes, respectively, are accumulated in the graphene layer. In top gated devices as shown in Fig. 1(b), the polymer electrolyte (liquid, ionic conductor) is put on the sample. For the polymer electrolyte, for example, we have used a mixture of lithium perchlorate ($LiClO_4$) and poly(methyl methacrylate) (PMMA, molar weight 120,000) with a weight ratio of 0.30:1, dissolved in propylene carbonate (PC) to form a precursor. For examples of other electrolyte solutions, see Refs. [9,10,51]. Once the precursor is ready for use, we apply it to the graphene device. The solvent from the precursor evaporates and a thin film of

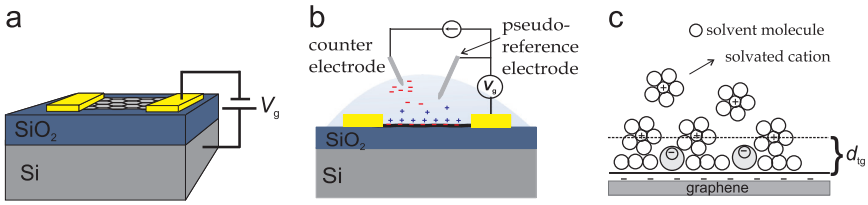

Fig. 1. (Color online) (a) Schematic view of the back gate graphene device. A variable voltage V_g can be applied between the graphene and the p-type silicon substrate. The device is treated as a parallel plate capacitor where the silicon oxide layer is the dielectric medium, (b) schematic view of top gate graphene devices using electrolyte solutions and (c) proposed model of the electric double-layer region, where d_{tg} is the Debye length.

transparent polymer electrolyte is formed on top of the device. The device can be baked at about 90 °C to remove residual moisture and alcohol. Since the polymer and the salt are dissolved in a solvent, the final material is liquid but it is very viscous and it does not evaporate with laser light exposure.

When the gate voltage V_g is applied between the sample and a counter electrode, positive (negative) ions from the electrolyte are accumulated near the graphene sample and they form an electric double layer (Fig. 1(c)) combined with the electrons (holes) in the graphene sample. In this case, we do not need any insulators to separate the negative and positive carriers since the ions of the double layer are surrounded by molecules which can work as an insulating layer for the electric double layer.

It is noted here that we will not discuss here the conventional top-gated semiconducting devices in which an insulating layer and then the top gate are deposited on top of the graphene sample. This type of top-gated device is essentially the same as the bottom gated devices, and such a device is not suitable for optical measurements whereby the incident light comes to the top of the sample.

The merits of the bottom gated device are (1) this is a well established technique in semiconductor technology and (2) such devices have a fast response to carrier accumulation. The merits of the top gate with electro-chemical doping are that: (1) there is no need to make any insulating layers (and thus it is easily fabricated), (2) the transparent top gate is suitable for Raman measurements. Another important merit of the top gate device is that (3) we can change the Fermi energy over a relatively wide range since the size of the solvent molecule is much smaller (several nm) than the width of the SiO_2 layers (100–300 nm) that are used in the bottom gated devices. The disadvantage of the bottom gate approach is that we cannot change the Fermi energy over a large energy range compared with the electro-chemical doping technique. If we make a very thin oxide layer on the order of a nm, the breakdown voltage of the insulator occurs at a relatively low V_g. The disadvantages of the top gate device with electro-chemical doping are: (1) the response of ions is much slower than the response of electrons or holes and (2) we need to cover the electrolyte with a protective layer if we want to use the device for real applications. Thus one or the other of the two devices can be selected in a complementary way depending on the purpose of the device. Hereafter, we discuss the relationship between the Fermi energy and the gate voltage for each case.

2.1. Back gated devices

The amount of charge induced in graphene can be modeled by considering the system as a parallel plate capacitor, where one plate is the planar graphene sheet and the other one is the conducting p-doped silicon substrate. The silicon dioxide layer works as the dielectric medium between the two conditions (see Fig. 1(a)). The geometric capacitance per unit area C_G of this system is given by

$$C_G = \frac{\varepsilon\varepsilon_0}{d}\ \mathrm{Fm}^{-2}, \tag{1}$$

where $\varepsilon_0 = 8.854\times10^{-12}\ \mathrm{Fm}^{-1}$ and ε are the permittivity of vacuum and of the SiO_2 layer, respectively, and d is the thickness of the SiO_2 layer. Then, the number of electrons per unit of area, n, transferred to the graphene by applying a voltage V_g is given by [11]

$$n = \frac{\varepsilon\varepsilon_0(V_g - V_0)}{ed} = 7.2\times10^{10}\ \mathrm{cm}^{-2}\ \mathrm{V}^{-1}\ (V_g - V_0), \tag{2}$$

where $e = 1.602\times10^{-19}$C is the electron charge. Here we have used $d = 300$ nm and $\varepsilon = 3.9$ for the silicon dioxide [12] and V_0 is a constant voltage to adjust the Fermi level to the Dirac point, *i.e.*, the charge neutrality point. The position of the Dirac point can be located by placement at the minimum in the conductivity between the source and the drain electrodes by appropriately varying the V_g.

The value of n in Eq. (2) is equal to the number of states per unit of area N/A in a two-dimensional system, which is given by [13]

$$n = \frac{N}{A} = \frac{gk_F^2}{4\pi}, \tag{3}$$

where N is the total number of states, A is the area of the unit cell in reciprocal space, $g = 4$ is the spin (up and down) and valley (K, K′) degeneracy, and k_F is the wavevector at the Fermi level. When we assume the linear dispersion $E_F = \hbar v_F k_F$, the Fermi energy E_F is written in terms of V_g from Eqs. (1), (2) and (3)

$$E_F = \hbar v_F\sqrt{\pi C_G|V_g - V_0|/e}. \tag{4}$$

When we use $C_G = 1.15\times10^{-4}\ \mathrm{F/m^2}$, $v_F = 1.0\times10^6$ m/s, and $V_g - V_0 = 1.0$ V, then we get $E_F = 31.2$ meV and the corresponding value of the Fermi wavevector becomes $k_F = 4.75\times10^{-3}\ \mathrm{\AA}^{-1}$.

2.2. Top gated devices with electro-chemical doping

Charges in monolayer graphene can also be induced by means of a top gate device. The advantages of using a polymer electrolyte are that the polymer electrolyte enables the application of large electric fields that are capable of inducing significant carrier densities over $10^{13}\ \mathrm{cm}^{-2}$. The transparency of the film makes it convenient for optical studies of graphene-based devices.

The polymer electrolytes are formed by dissolving salts in soft polymeric materials. The electric conduction mechanism involves the motion of oppositely charged ions in opposite directions in the polymer matrix. At the electrode–polymer interface, the ion flow is intentionally stopped before chemical reactions could occur at the interface. An electrical double layer (also known as a Debye layer) of opposing charges is then formed between the gate material and the polymer matrix material as shown in Fig. 1(c), and the electrical double layer is maintained as long as the gate voltage does not exceed the threshold for electrochemical reactions (~1.5–2.0 V in our case). The distance between the oppositely-charged layers at the electrodes is given by the Debye screening length which is typically on the order of a few nanometers [14]. Because of the small Debye length, the geometric capacitance of the system (Eq. (1)) is much larger than that in usual back gated devices using Si/SiO_2, where the distance between the two oppositely-charged layers is about 300 nm. Consequently, the graphene sample can be charged with a one order of magnitude higher density of carriers.

The application of a gate voltage V_g creates an electrostatic potential difference ϕ between the graphene and the gate electrode, and the addition of charge carriers leads to a shift in the Fermi level E_F. Therefore, V_g is given by

$$V_g = \frac{E_F}{e} + \phi, \tag{5}$$

with E_F/e being determined by the chemical (quantum) capacitance of the graphene, and $\phi = ne/C_G$ being determined by the geometrical capacitance C_G [15]. In classical electromagnetism, all positive and negative charges appear at the surface of a metal and the electric field inside of the metal is zero because of complete screening by these surface charges. The capacitance thus obtained is called a geometrical capacitance. However, since the graphene is one atomic layer thick, the electric field created by the gate is only partially screened and thus the capacity becomes less than the geometrical capacitance. The capacitance obtained when considering such a screening effect is called the quantum capacitance.

In the back gate device, the graphene on a Si/SiO_2 substrate with 300 nm of SiO_2 has a small geometric capacitance per unit area $C_G = 1.15 \times 10^{-8}$ F cm^{-2} (Eq. (1)). Thus, for a typical value of the carrier density $n = 1 \times 10^{13}$ cm^{-2}, the potential drop becomes $\phi = 140$ V, which is much larger than E_F/e~0.37 V for monolayer graphene and the contribution from E_F/e in Eq. (5) can then be neglected. Thus in the case of the back gated (bg) device, $V_{bg} \approx \phi$ and the doping concentration n is expressed simply by $n = \eta V_{bg}$, where $\eta = C_G/e$ is a factor that shows that the carrier density can be accumulated by a given V_{bg}.

Similar to the back gated systems discussed above, top gated systems can also be modeled as a parallel-plate capacitor, but now the Debye layer is the dielectric layer made of polymer molecules whose thickness is a few nanometers (~1–5 nm) [15]. As an example, assuming a Debye length of 2 nm, and taking the dielectric constant ε of the polymer PEG to be ~5 [15] or of PMMA to be ~2.6 [16], we obtain a gate capacitance per unit area $C_G = 2.2 \times 10^{-6}$ F cm^{-2} for PEG and $C_G = 1.2 \times 10^{-6}$ F cm^{-2} for PMMA, which is 100 times larger than the geometric capacitance for the back gate system. In this case, the first term in Eq. (5) cannot be neglected.

Substituting $\phi = ne/C_G$ and Eq. (2) for n and Eq. (4) for E_F into Eq. (5), we get

$$V_g = \frac{\hbar v_F \sqrt{\pi n}}{e} + \frac{ne}{C_G}. \tag{6}$$

Using the numerical values $C_G = 2.2 \times 10^{-6}$ F cm^{-2} and $v_F = 1.0 \times 10^6$ m/s, we obtain a relation for V_g in terms of the doping density n as

$$V_g = 1.16 \times 10^{-7} \sqrt{n} + 0.728 \times 10^{-13} n, \tag{7}$$

where n is in units of cm^{-2}. For example, for $V_g = 1$ V, we get a value of $n = 9 \times 10^{12}$ cm^{-2}, and $E_F = 0.35$ eV for this top gated device. The back gate and top gate devices discussed in Section 2 are used experimentally to vary the carrier density and the Fermi level in realizing the physical concepts involved in using Raman spectroscopy to study phonon renormalization in metallic nanotubes and graphene.

Finally it is noted that the two type of gates (solution gated and electrostatically gated) have a different sign convention for carriers on a graphene sample for a given gate voltage. For *a positive gate voltage*, electrons are accumulated on graphene for the bottom gate measurements, while holes are accumulated on graphene for the top gate measurements. Likewise, for *a negative gate voltage*, holes are accumulated on graphene for the bottom gate measurements and electrons are accumulated for the top gate measurements. It worth mentioning that the different conventions are needed because the top gate voltages are applied through a potentiostat device (in this case the graphene flake is not grounded), while the back gate voltages are applied through a DC source generator, in which the graphene is grounded.

3. The Kohn anomaly

The formalism used to describe phonon renormalization is called the Kohn anomaly which is the most important for determining the phonon frequency and line width in graphene and metallic carbon nanotubes and both quantities are measured in a Raman scattering measurement. More generally, the Kohn anomaly is a phonon softening phenomena in the presence of the free electrons in a metallic energy band. In the normal metal, only electrons at the Fermi energy with the wavevector $-k_F$ can be excited by absorbing a phonon through the electron–phonon interaction. In the case of graphene and metallic carbon nanotubes, the final states are generally unoccupied states in the same metallic energy band with a wavevector k_F and with phonon wavevectors that are thus $2k_F$ (as shown in Fig. 2(a)). The opposite relaxation process from k_F to $-k_F$ is possible, too, if the state at $-k_F$ is not occupied. Using second order perturbation theory, the phonon energy is expressed by [8]

$$\hbar\omega_{\mathbf{q}} = \hbar\omega_{\mathbf{q}}^{(0)} + 2\sum_{\mathbf{k}\mathbf{k}'} \frac{|V_{\mathbf{k}\mathbf{k}'}|^2}{\hbar\omega_{\mathbf{q}}^0 - E^{eh} + i\gamma_{\mathbf{q}}/2} \times (f_h - f_e) \tag{8}$$

where $\mathbf{k}$ and $\mathbf{k}'$ are, respectively, wave-vectors for the initial and final electronic states; $\mathbf{q} \equiv \mathbf{k} - \mathbf{k}'$ is the phonon wave-vector; $E^{eh} \equiv (E^e_{\mathbf{k}'} - E^h_{\mathbf{k}})$ is the e–h pair energy; $\omega_{\mathbf{q}}^{(0)}$ is the phonon frequency; $\gamma_{\mathbf{q}}$ is the phonon decay width; $f_h(f_e)$ is the Fermi distribution function for holes (electrons) and $V_{\mathbf{k}\mathbf{k}'}$ gives the electron phonon matrix element. For a specific phonon frequency $\omega_{\mathbf{q}}$, the phonon frequency correction term due to its self-energy is given by $\hbar\omega_{\mathbf{q}} - \hbar\omega_{\mathbf{q}}^{(0)} \equiv [\Pi(\omega_{\mathbf{q}}, E_F)]$. Here $\Pi(\omega_{\mathbf{q}}, E_F)$ is a complex quantity with a real part that is a shift of the phonon energy $\hbar\omega_{\mathbf{q}} - \hbar\omega_{\mathbf{q}}^{(0)}$, where $\hbar\omega_{\mathbf{q}}^0$ is the phonon energy in the adiabatic approximation. The imaginary part $\mathrm{Im}[\Pi(\omega_{\mathbf{q}}, E_F)]$ of Eq. (8) gives the decay width, $\gamma_{\mathbf{q}}$, which determines the inverse lifetime of the phonon [8]. The $\gamma_{\mathbf{q}}$ is determined self-consistently in the sense that the imaginary part of $\hbar\omega_{\mathbf{q}}$ is $\gamma_{\mathbf{q}}$.

In a normal metal, the phonon energy at $q = 2k_F$ becomes soft because the energy denominator of Eq. (8) becomes negative since E^{eh} for a given q is larger than $\hbar\omega_{\mathbf{q}}^0$. Phonon softening at $q = 2k_F$ can be observed experimentally by inelastic neutron scattering measurements. This phenomenon in a three dimensional metal is generally called the Kohn anomaly [7]. Especially for one-dimensional metals (or low dimensional materials) with a "nesting Fermi surface" (parallel Fermi surfaces of k_F and $-k_F$), the Kohn anomaly can become significant. In fact, the phonon frequency $\hbar\omega_{\mathbf{q}}$ can obtain a negative (or more correctly a pure imaginary) value, and this situation is called the giant Kohn anomaly. In the case of

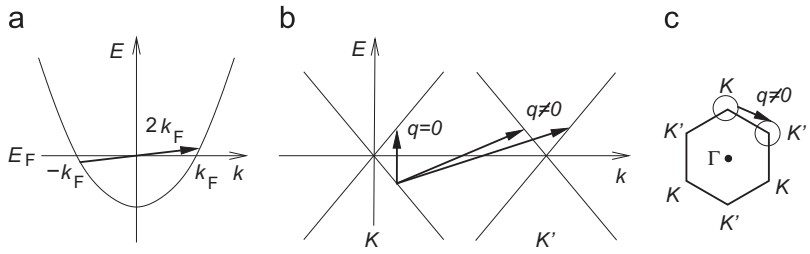

Fig. 2. The Kohn anomaly, (a) in the case of a normal metal, an electron is excited from $-k_F$ to k_F by absorbing a $q = 2k_F$ phonon. If we consider the second order perturbation process for a phonon, the phonon energy with $q = 2k_F$ becomes soft, (b) in the case of graphene, an electron is excited from the π to π^* band within the same k by absorbing a $q = 0$ phonon which becomes soft. There is another possibility of the excitation for $q = KK' = \Gamma K$ for the scattering from one valley K to another valley K′ (intervalley scattering), (c) the two dimensional Brillouin zone of graphene and the circles represent equi-energy circles around the K and K′ points. An arrow shows the intervalley scattering.

the giant Kohn anomaly, the lattice becomes distorted (Peierls' instability) and a charge density wave (CDW) for the electronic charge appears.

In the case of undoped graphene, since there are occupied π and unoccupied π^* energy bands that touch each other at the Dirac point which coincides with the Fermi energy, a phonon with $q=0$ (Fig. 2(b)) can excite an electron only from the π to π^* band. Further, since the slope of the phonon energy dispersion is much smaller than the slope of the electron energy dispersion, only q~0 phonon excitation is allowed within a Dirac cone. However, in the hexagonal Brillouin zone of graphene, as shown in Fig. 2(c), there are two inequivalent hexagonal corners in k space, so that we expect electron excitation from π at the Dirac cone around the K point to be scattered to π^* at the Dirac cone around the K′ point as shown in Fig. 2(b). This scattering process of an electron (or hole) is called intervalley (EV) scattering, while the scattering within the same Dirac cone is called intravalley (AV) scattering [17]. In the case of EV scattering, the phonon wave vector q corresponds to ΓK and either the phonon near the K point or a phonon near the K′ point is relevant. In Section 4, we will discuss the combination phonon modes corresponding to the EV scattering processes. Hereafter in this section, we discuss AV $q=0$ phonons.

The zone-centered $q=0$ phonon softening phenomena can be observed by Raman spectroscopy as a phonon frequency change and a spectral width broadening. The spectral width broadening occurs because the phonon now has a finite life time which comes from the interaction of the phonon with electrons. This interaction occurs because the phonon frequency of the optical phonon mode is relatively high (47 THz, 20 fs) compared with the time for the electron–phonon interaction time (~100 fs) estimated by the uncertainty relation. Quantum mechanics tells us that an elementary excitation with a finite life time behaves like a "quasiparticle". In the presence of an electron–phonon interaction, a phonon at $q=0$ in graphene becomes such a quasiparticle.

In the case of m-SWNTs, the LO phonon mode (G band) which is seen in the Raman spectra at a frequency of 1590 cm^{-1} for s-SWNTs becomes soft for m-SWNTs and is observed around 1550 cm^{-1}, but with a frequency that depends on the nanotube diameter. In the Raman spectra of a single wall carbon nanotube (SWNT), the two in-plane optical phonon modes, that is, the longitudinal and in-plane transverse optical (LO and iTO) phonon modes at the Γ point at the center of the hexagonal, two-dimensional Brillouin zone (2D BZ), which are degenerate in graphene, split into two peaks, G^+ and G^- peaks, respectively, due to the curvature of the cylindrical nanotube surface [4,18,19]. Since the splitting of the two peaks for SWNTs depends on the nanotube curvature, the frequency between the G^+ and G^- modes is thus inversely proportional to the square of the diameter d_t of SWNTs (curvature). For the case of s-SWNTs, the G^+ mode does not change with changing d_t because the vibration is parallel to the nanotube axis, but the G^- frequency, whose vibration is perpendicular to the nanotube axis, decreases with decreasing d_t [20]. In the case of m-SWNTs, the G peak for the LO mode G^- appears at a lower frequency than the G peaks for the iTO mode G^+ [21]. The spectra of G^- for metallic SWNTs show a much larger spectral width than that for semiconducting SWNTs. Furthermore, the spectral G^- feature shows an asymmetric lineshape as a function of frequency which is known as the Breit–Wigner–Fano (BWF) lineshape and is expressed by the following formula [22]:

$$I(\omega) = I_0 \frac{[1 + (\omega - \omega_{\mathrm{BWF}})/q_{\mathrm{BWF}}\Gamma_{\mathrm{BWF}}]^2}{1 + [(\omega - \omega_{\mathrm{BWF}})/\Gamma_{\mathrm{BWF}}]^2}, \tag{9}$$

where $1/q_{\mathrm{BWF}}$ is an asymmetry factor and ω_{BWF} is the BWF peak frequency at maximum intensity I_0, while Γ_{BWF} is the half width of the BWF peak. If $1/q_{\mathrm{BWF}} = 0$, then $I(\omega)$ shows a Lorentzian lineshape and thus the function Eq. (9) is a natural extension of the spectral function. The origin of the asymmetric lineshape is the interference effect (the Fano effect) of the discrete (phonon) states with the continuous (electron excitation) spectra [23].

The Kohn anomaly effects depend on the Fermi energy since the Fermi distribution function in Eq. (8) is modified by the self-energy correction term [24] if optical processes in the perturbation expansion are suppressed by occupying an unoccupied state (or unoccupying the occupied state) with increasing (decreasing)

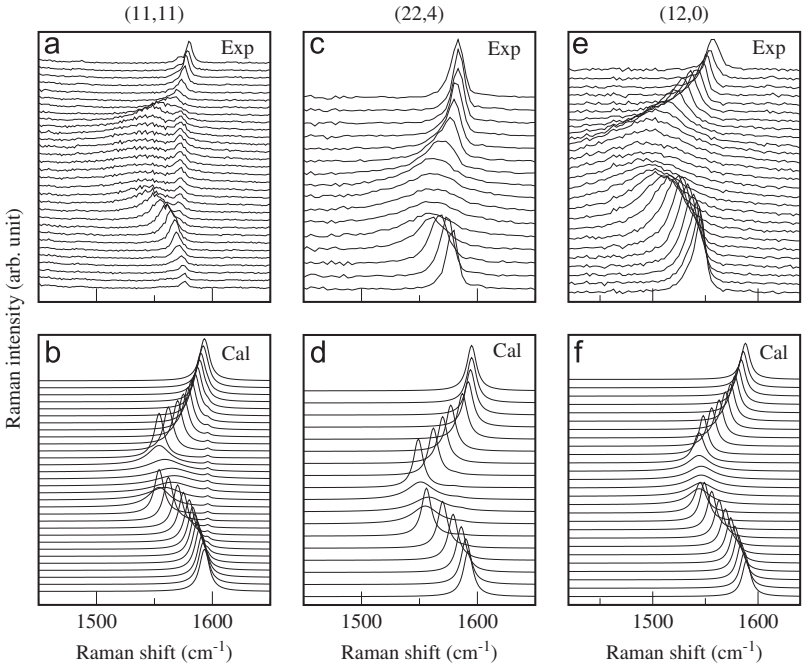

Fig. 3. (a), (c), (e) Experimental G band Raman spectra which are given for various values of V_g, taking advantage of the electro-chemical doping effect. (a) $V_g = 1.5$ to −1.5 V, (c) $V_g = 1.9$ to −1.3 V, (e) $V_g = 1.3$ to −1.3 V. (b), (d), (f) Calculated G band Raman spectra taken by changing the Fermi energy E_F from (b) 0.45 to −0.45 eV, (d) 0.60 to −0.42 eV, and (f) 0.39 to −0.39 eV. Nanotube chiralities are: (a) and (b) (11, 11), (c) and (d) (24, 4), (e) and (f) (12,0), and adjacent curves differ by $\Delta V = 0.1$ V. Taken from Ref. [27].

Fermi energy which can be accomplished through the use of an applied gate voltage. When E^{eh} is smaller (larger) than $\hbar\omega_{\mathbf{q}}^0$ in the denominator of Eq. (8), the corresponding processes contribute to the phonon hardening (softening) [25]. Thus the suppression of the lower energy excitation below $\hbar\omega_{\mathbf{q}}^0$ by increasing or decreasing the Fermi energy causes the phonon frequency to become soft and to have a minimum at $E_F = \pm\hbar\omega_{\mathbf{q}}^0/2$. The Fermi energy dependence of $\omega_{\mathbf{q}}$ can be clearly observed at a low temperature (10 K), since the Fermi distribution becomes a step function of energy [26]. Further, the Kohn anomaly of m-SWNTs is shown for various values of the gate voltage V_g in Fig. 3 where the Kohn anomaly is seen to have a nanotube chirality dependence.

In Fig. 3, we also show the calculated Raman spectra (below) as a function of the Fermi energy for (b) (11,11) armchair, (d) (22,4) chiral and (f) (12,0) zigzag m-SWNTs, which reproduces the experimental Raman spectra well for m-SWNTs of the same chirality, respectively, in Fig. 3(a), (c) and (e) (above). The reason why the Kohn anomaly effect depends on the chirality is that the electron–phonon (more precisely exciton-phonon) interaction is k dependent around the K point in the two-dimensional Brillouin zone (for details see Refs. [25,27,28]).

We can also see the Kohn anomaly effect in the Raman spectra for the radial breathing phonon modes (RBM) [29], but the phonon softening effect is small (2–3 cm^{-1}) for the RBMs because: (1) the phonon energy of a RBM is much smaller than for the G band and (2) the time period of vibration (100–200 fs) is even longer than the time period for the electron–phonon interaction (100 fs) [8].

In the case of graphene, the optical mode also shows a Kohn anomaly effect [15] but the broadening and asymmetry are not so large when the Fermi energy is located at the Dirac point because the electronic density of states of graphene at the Dirac point is zero while the density of states of m-SWNTs at the Dirac point is finite. The difference in the density of states behavior in graphene and in carbon nanotubes comes from the different dimensionality of the two systems. When the Fermi energy is shifted from the Dirac point in graphene, we can see some asymmetry in the Raman spectra.

In the case of graphite, when we intercalate many alkali metal ions between graphene layers (to form graphite intercalation compounds (GICs) [31]) we can also observe BWF line shapes. The asymmetric shape in GICs depends on the stage number [30] as shown in Fig. 4. Here the stage number n is defined by the number of graphene layers between subsequent alkali metal ion layers. Stages 1, 2 and 3 Rb intercalated GICs correspond, respectively, to the C_8Rb, $C_{24}Rb$, and $C_{36}Rb$ stoichiometries. In stage n GICs, a layer of ions is intercalated between every n graphene layers. With decreasing stage number from 3 to 1, the shift and broadening of the G-band increases and in the case of stage 1, we can clearly see an asymmetric Raman lineshape. It is pointed out here that in the case of GICs with higher stage than 2, the electrons donated from the alkali metal ions to the graphene layers are inhomogeneously distributed in the direction perpendicular to the graphene plane, and thus the Fermi energies of the bounding layer adjacent to the intercalate layer and E_F for the internal graphene layers measured from the Dirac point are not the same as one another. That is, the bounding graphene layer close to the intercalate layer is strongly perturbed, but the interior layers are only weakly perturbed. Thus we need to consider the contributions to the Raman spectra from both the bounding and interior layers separately in the analysis of the Raman spectra [31].

4. The Kohn anomaly for the $q\neq0$ phonon of graphene

In this section, we only discuss the Kohn anomaly for $q\neq0$ phonons in terms of gate modulated Raman spectroscopy.

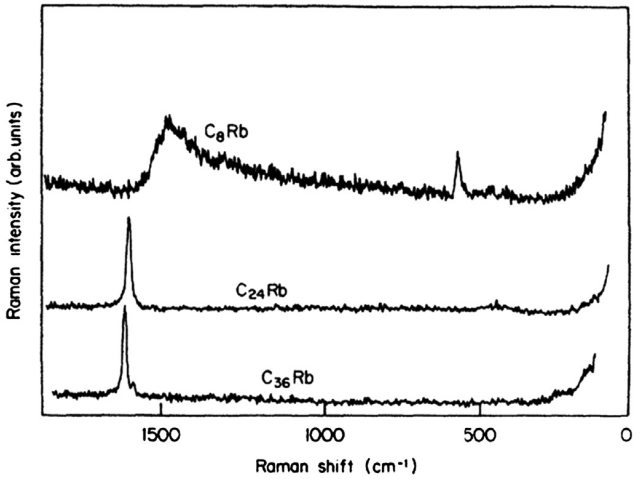

Fig. 4. Raman spectra of C_8Rb (stage 1), $C_{24}Rb$ (stage 2), and $C_{36}Rb$ (stage 3) graphite intercalation compounds. In the case of the C_8Rb, the G band spectrum is significantly softened and shows an asymmetric lineshape with a peak intensity around 1400 cm^{-1}. The figure is taken from Ref. [30].

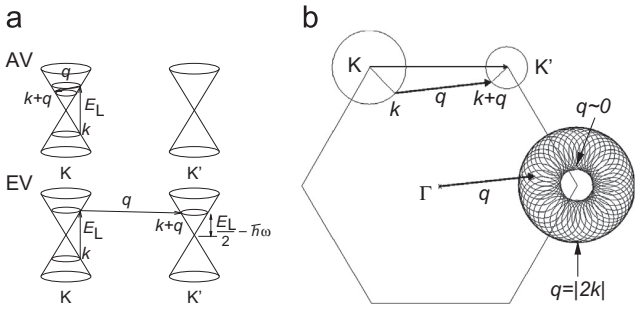

Fig. 5. (a) The intravalley (AV) and intervalley (EV) scattering process of a photo excited electron. A photo-excited electron at **k** on an equi-energy circle of a Dirac cone around the K point in the hexagonal Brillouin zone is scattered to a **k**+**q** state on another equi-energy circle around a K or K′ point, respectively, for an AV or EV process by emitting a phonon with −**q**. (b) The $q=0$ and $q=2k$ conditions of double resonance Raman spectroscopy. For a given **k** point, many **k**+**q** states are possible on a circle. When we rotate **k** around an equi-energy line near the K point, the circles of **k**+**q** are rotated around the K point if we plot the **q** vector from the Γ point. When we consider the phonon density of states for such a q vector, the inner q~0 and outer $q=|2\mathbf{k}|$ vectors becomes singular, which we identify as the $q=0$ and $q=2k$ conditions for double resonance Raman spectroscopy.

As shown in Fig. 2(c), there are two Dirac cones around the two inequivalent hexagonal, two-dimensional Brillouin zone corners, the K and K′ points. For a given electron–hole (e–h) pair energy excited by a $q\neq0$ phonon, there are two possible scattering processes, namely intravalley (AV, $q=0$ and q~0) and intervalley (EV, $q\neq0$) (Fig. 5(a)) scattering [17]. For the one phonon Raman spectra, only $q=0$ occurs and thus only AV phonon scattering can be observed, because after the scattering of a photo-excited electron at $k+q$ that electron should be recombined with a hole at k, which requires the condition that $q=0$. However, for two phonon Raman spectra, the $q\neq0$ phonon scattering for both AV and EV processes is possible, and we can observe either overtone or combination phonon modes for either of the two AV or EV processes with q and $-q$. It is however noted that a combination mode between an AV and an EV phonon is not possible since we must select the pair of q and $-q$ phonons for a combination mode.

In two phonon Raman spectroscopy, an important concept is the enforcement of the double resonance conditions for the phonon wavevector q, that is, $q=2k$ and q~0 in which k is the absolute value of the electron wavevector measured relative to the K point [3,19,32], as shown in Fig. 5(b). In Fig. 5(a) and (b), we

show an equi-energy circle for electron wavevector **k** around the K point where optical absorption occurs for a given laser energy E_L. If we assume that the π and π^* energy bands are symmetric around the Dirac point energy, then we obtain, $E(k) = \pm\sqrt{3}\gamma_0 ka$ (γ_0 is the nearest neighbor tight binding energy, a is the lattice constant, and $k = |\mathbf{k}|$.), In this case, the energy of the photoexcited electron is $E_L/2$ measured from the Dirac point energy and thus $k = E_L/2\sqrt{3}\gamma_0 a$. For a given **k**, the photo-excited electron scatters to **k**+**q** states at the K′ point by emitting a **−q** phonon (EV scattering, Fig. 5(b)). The possible **k**+**q** states are then on another equi-energy circle with an energy of $E_L/2-\hbar\omega(-\mathbf{q})$ in which the phonon energy $\hbar\omega(-\mathbf{q})$ is much smaller than E_L and thus we can make the approximation that the two circles have the same diameter. When we plot **q** for a given **k** measured from the Γ point, the vector moves on a circle near the K point and when we rotate **k** around the K point, then the circles rotate around the K point forming a donut shape, as shown in Fig. 5(b). In the case of Fig. 5(b), the outer $q = 2|\mathbf{k}|$ and inner q~0 regions give a singularity in the phonon density of states for the EV scattering phonons. Thus in the two phonon Raman spectra, phonons at $q=2k$ or q~0 are observed. When we increase E_L, k also increases and the observed phonon energy for $q=2k$ changes along the phonon dispersion curve, which we call the "dispersion of the Raman spectra". On the other hand, the observed phonon energy for $q=0$ does not depend on E_L [32].

Thus even though there are many possible **q** vectors which are involved in the two phonon scattering process, the observed phonon in the Raman spectra has a wave vector that is either $q=2k$ or q~0. The corresponding Raman spectra is further enhanced by the "double resonance" process in which two out of the three intermediate states are real electronic states, so that the corresponding double resonance Raman intensity becomes comparable or even stronger than the first order resonance Raman intensity. The double resonance Raman process which is very important in the Raman spectra observed for graphene and nanotubes (see more in Ref. [19]) because the electron–phonon interaction is not only strong near the Γ point but the spectra are also very strong near the K (or K′) points [17]. If we are now considering the Raman spectra for the defect-induced peaks, such as the D, and D′ bands, then one of two scattering processes is an elastic scattering by a defect and the double resonance theory can also be applied to understand the defect-induced Raman spectra [3,19].

When we assign the phonon modes for a given Raman spectrum of graphene, we will consider the following four conditions: (1) we select overtone or combination modes of the phonon from six phonon modes; oTA, iTA, LA, oTO, iTO and LO; (2) we select either single or double resonance Raman spectra, and in the case of the double resonance spectra, we select either (defect-induced elastic scattering)+(a phonon) or two phonon Raman spectra; (3) we select either AV or EV scattering processes; and (4) we select either $q=0$ or $q=2k$ double resonance conditions. For first order Raman processes, only the iTO and LO phonons are Raman active and these scattering processes both give a G band signal around 1580 cm^{-1}. In the case of SWNTs, the radial breathing mode (RBM) can be seen as the first order Raman spectra, and the RBM frequency is inversely proportional to the nanotube diameter [33]. In the second order processes, we have 6×6 combinations of phonon modes, 2 scattering processes (AV or EV), 2 double resonance conditions (q~0 or $q=2k$) and thus 144 possible combination or overtone phonon modes. The method for assigning the overtone and combination modes are given by the following three conditions: (1) sum of the frequency is close to the phonon modes at Γ (AV) or K (EV), (2) when we change the incident laser energy (E_L), the $q=2k$ double resonance phonon mode frequency changes according to the dispersion as is discussed above [32], while the $q=0$ double resonance or single

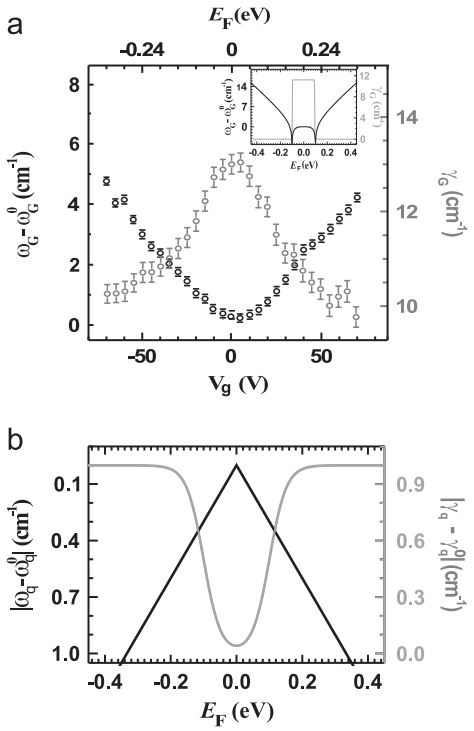

Fig. 7. (a) V_g−dependence of the phonon frequency correction $\omega_G-\omega_G^{(0)}$ (black line) and the corresponding decay width change of $\gamma_{\mathbf{q}}-\gamma_{\mathbf{q}}^{(0)}$ (grey line) for the G band. The inset shows the corresponding theoretical illustration and (b) illustrative predictions for the V_g−dependence of the phonon frequency correction $\omega_G-\omega_G^{(0)}$ (black line) and the corresponding decay width change of $\gamma_{\mathbf{q}}-\gamma_{\mathbf{q}}^{(0)}$ (grey line) for the $q\neq0$ phonons. The behaviors of the frequency and spectral width are opposite to the case of (a) [38].

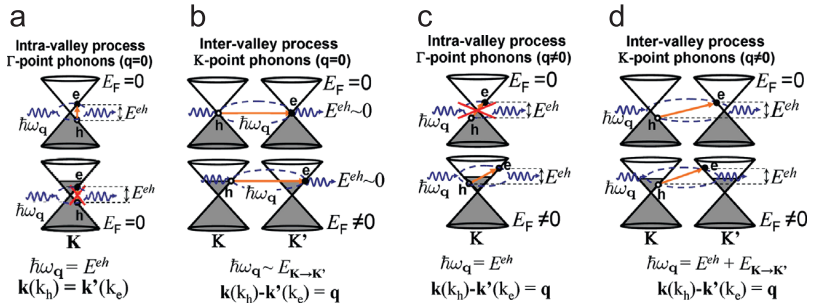

Fig. 6. (Color online) (a) Intravalley (AV) scattering with Γ−point phonons ($q=0$) processes for e–h pair creation due to phonon (with energy $\hbar\omega_{\mathbf{q}}$) absorption. E^{eh} stands for the e–h pair energy, (b) intervalley (EV) scattering with a K point phonon ($q=0$ measured from the K point), (c) AV scattering with a $q\neq0$ phonon and (d) EV scattering with a $q\neq0$ phonon [38]. $E_F=0$ (top line) and $E_F\neq0$ (bottom line) are shown.

resonance Raman frequency does not change and (3) when a Raman signal becomes strong for defective graphene, the corresponding Raman signals (D and D′) are defect induced Raman signals. In this article, we will explain how gate modulated Raman spectroscopy provides a new technique for the assignment of the combination and overtone phonon modes.

Most of the discussions in the literature until now for the phonon self-energy corrections have been for zone-center phonons (Γ point) with $q=0$ by observing the G-band Raman spectra in monolayer graphene (1LG) as a function of the Fermi level energy (E_F) or of the gate voltage (V_g) [29,34–37]. In Fig. 6(a) we show the corresponding perturbation process for the $q=0$ phonon which can be suppressed by increasing $|E_F|$ [38]. The phonon frequency ω_G and its corresponding spectral width γ_G are shown in Fig. 7. These experimental results are explained by the conventional theory of the Kohn anomaly [35–37,39], which shows a ω_G hardening and γ_G narrowing when $|V_g|$ increases as a function of E_F.

The double resonance Raman features with frequencies ranging between 2350 and 2850 cm^{-1} (which contain the G* (2450 cm^{-1}) and the G′ (or 2D, around 2700 cm^{-1}) bands, as shown in Fig. 8(a), were studied to show that the phonon renormalization for $q\neq0$ phonons gives a different E_F dependence from that for the G band and this effect can be used in making specific phonon assignments. Figs. 7 and 8(a)–(d) show the experimental results.

The G* and G′ bands are the most prominent double-resonance features in the Raman spectra in graphene and an assignment of the G* band at 2450 cm^{-1} was not yet well solved in prior publications. Originally, the G* band had been assigned to the 2iTO phonon overtone mode (q~0, EV) [40] and then Mafra et al. assigned the G* band as the iTO+LA phonon combination mode ($q=2k$ EV), since they observed a dispersion in the Raman spectra of −18 cm^{-1}/eV by changing E_L [41].

Let us now understand what happens for phonons corresponding to the cases for the q~0 EV and $q=2k$ AV/EV scattering processes. As shown in Fig. 8(b)–(d), the G* and the G′ bands show a different behavior when $|V_g|$ increases compared to the behavior observed for the AV $q=0$ process. Regarding the G* band, we assign it in Fig. 8 as the ITO+LA and the 2iTO in which the frequency of the iTO+LA mode ω_{iTO+LA} decreases with increasing $|V_g|$, while their decay width γ_{iTO+LA} increases with increasing $|V_g|$. For the 2iTO G* feature at ~2470 cm^{-1}, which is a $q=0$ EV process around the K point (Fig. 8(c) and (d)), the frequency ω_{2iTO} and the decay width γ_{2iTO} almost do not change with increasing $|V_g|$. These results mean that there are two Raman peaks around 2450 cm^{-1} involving different laser excitation processes even though they almost overlap with each other in frequency. These conclusions follow from the ability to use both gate modulation and different laser excitation energies strategically to show a different physical process responsible for these two peaks. A phenomenological formulation for the phonon self-energy for the EV $q=0$ and the AV/EV $q=2k$ processes in single-layer graphene is presented to explain the anomalous experimental results and the way that variation of V_g and of the laser excitation energy cooperatively can be used to assign phonons. If we remember the case of the AV processes for the $q=0$ phonons (Fig. 6(a)), which applies to the G-band feature (Fig. 7(a)), the creation of an e–h pair is possible when $E_F=0$, which implies a ω_q softening and a γ_q broadening. With increasing $|E_F|$, ω_q hardens and γ_q narrows, which means that the e–h pair excitation is suppressed by the Pauli principle because the phonon energy is becoming smaller than 2 $|E_F|$ [39,42]. This approach can also now be used to understand the q~0 and $q=2k$

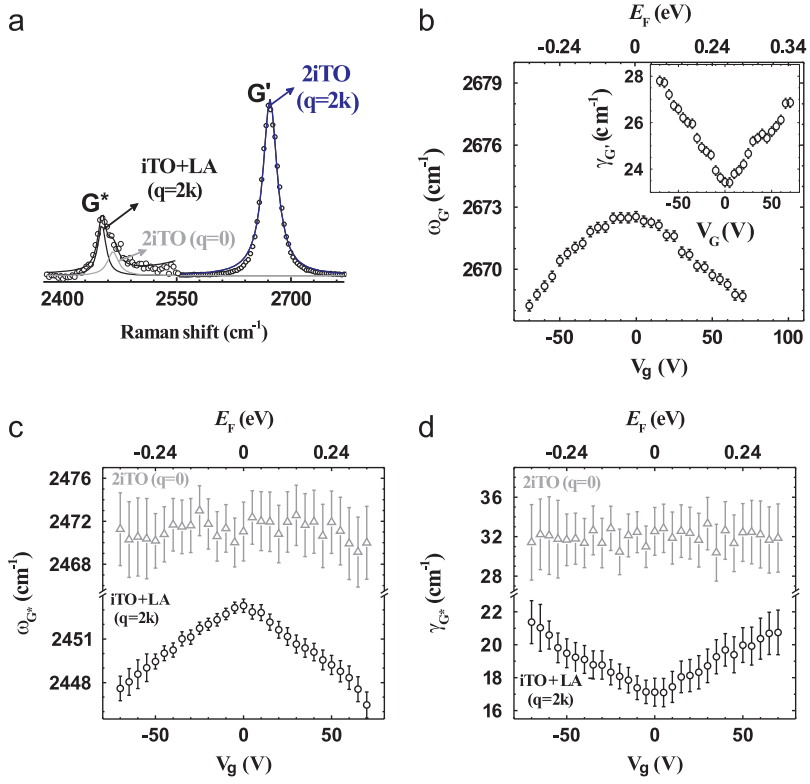

Fig. 8. (Color online) (a) The experimental Raman spectra of the G* and the G′ bands. The asymmetric G* feature is a combination of the iTO+LA modes ($q=2k$ read from the K point) and the 2iTO mode (q~0 read from the K point). The G′ mode is an overtone of the iTO mode ($q\approx2k$). For illustrative purposes, the signal of the G* feature was multiplied by a factor of 10 and the Lorentzian profiles used to fit the spectrum are shown in constructing (a), (b) the gate voltage V_g and Fermi energy dependence of the 2iTO ($q=2k$) $\omega_{G'}$ mode and $\gamma_{G'}$ values (inset in (b)), (c) and (d) show, respectively, the ω_q and γ_q dependencies on gate voltage and E_F seen for the iTO+LA and 2iTO modes (G* band). The error bars come from the fitting procedure [38].

processes by considering a small difference in approach: now, instead of the Pauli principle, the density of phonon and electronic states, as well as the energy and momentum conservation requirements, will be jointly responsible for suppressing the e–h pair excitation [38].

As shown above, a different behavior is expected for the q~0 phonon (measured from K-point) in the EV process shown in Fig. 6 (b), which explains the G* 2iTO mode behavior as $|E_F|$ is varied with varying $|V_g|$, shown in Fig. 8(a) and (b). According to the Fermi golden-rule, the probability that a real electron–hole pair exists at $E_F = 0$ (upper panel of Fig. 6(b)–(d)) is quite small since the density of states of both electrons and phonons at $E_F = 0$ almost vanishes [2,34]. Therefore, neither softening of $\omega_{\mathbf{q}}$ nor broadening of $\gamma_{\mathbf{q}}$ is expected, since almost no e–h pairs are excited. When $|E_F|$ increases (lower panel in Fig. 6(b)–(d)), the probability for a K point q≈0 phonon to connect inequivalent energy $\mathbf{k}$ and $\mathbf{k}'$ states increases, because the density of phonon and electron states also increases as we move away from the K point [2,34]. As a result, the number of e–h pair increases and the phonon mode softening and damping effects could be observed with increasing $|E_F|$. This means that the phonon self energy will be a small correction and, therefore, small $\omega_{\mathbf{q}}$ softening and small $\gamma_{\mathbf{q}}$ damping effects are expected for any $|E_F|$ value (weak E_F−dependence).

By considering phonon modes with $q = 2k$ AV and EV processes, as shown in Fig. 6(c) and (d), the phonon wavevectors are either around the Γ point or around the K point. Since the phonon and electron density of states are small close to the K point and since the phonon energy dispersion for graphene has a much smaller slope $\partial\hbar\omega_q/\partial q$ than that for the electronic energy dispersions $\partial E(k)/\partial q$ [2], there is essentially no coupling between q≠0 phonons and e–h pairs (since there is no $\mathbf{q}$ value such that $\mathbf{q} = \mathbf{k}-\mathbf{k}'$) if $E_F = 0$ and therefore the softening and damping of the phonon mode does not take place resonantly, *i.e.*, where $E^{eh} = \hbar\omega_{\mathbf{q}}$. However, when E_F≠0, the density of phonon and electron states increases and phonon modes with $q = 2k$ can now connect electronic states with different $\mathbf{k}$ and $\mathbf{k}'$ values, in the sense that there is a $\mathbf{q}$ such that $\mathbf{q} = \mathbf{k}-\mathbf{k}'$ (the different slopes between $\partial\hbar\omega_q/\partial q$ and $\partial E(k)/\partial q$ decrease when we move away from the K point [2]). This gives rise to a strong electron–phonon coupling which enhances the creation of real e–h pairs. As a consequence, the phonon mode softens ($\omega_{\mathbf{q}}$ decreases) and gets damped ($\gamma_{\mathbf{q}}$ broadens). This $q = 2k$ AV/EV process behavior is illustrated in Fig. 7(b), where it is seen that the frequency softening (black solid line) must increase with increasing $|E_F|$ while the decay width (grey solid line) must broaden with increasing $|E_F|$.

4.1. The combination modes around 1700–2300 cm^{-1}

Recently, attention has been given to studying some weak Raman features in the frequency range $1700 < \omega < 2300$ cm^{-1} (Fig. 9), which are associated with Raman combination and overtone modes of graphene [45–47]. These combination and overtone modes are seen in various forms of nano carbons but have not been studied systematically until recently. Firstly, the study of these modes in graphene is desirable for establishing a baseline that can be applied later to other nano carbons. Historically, laser excitation energy (E_L) dependent Raman spectroscopy has been used to perform the phonon assignments of these features, as is the case in the Refs. [45–47]. However, these works [45–47] disagree with each other regarding the number of phonon peaks and the phonon assignments attributed to each peak. The main reason behind this disagreement is that, by performing only E_L−dependent Raman experiments, it is not easy to properly assign the combination modes when these combination modes are close together in frequency and the spectral feature often overlap in their lineshape profiles. Moreover, an experiment limited to E_L-dependent measurements does not tell us in which directions in k space the various scattering processes are happening.

Concerning single layer graphene (1LG), the first studies of the combination modes in the frequency region between 1690 and 2150 cm^{-1} was reported by Cong et al. [46] and Rao et al. [45], while Cong et al. assigned only three peaks and Rao et al. reported two additional peaks. Recently, Mafra et al. [44] proposed a different assignment for some of these five peaks and showed that the $\mathbf{k}$-dependent electron–phonon interaction investigated by studying the Raman spectra as a function of both the Fermi energy E_F and gate voltage V_g by varying of both E_F and V_g is important to give accurate/reliable information about these combination modes.

Fig. 9(a) shows the combination modes in the spectral region from 1700 to 2300 cm^{-1} for four different laser lines: 488 nm, 532 nm, 575 nm and 590 nm. Five peaks could be observed in this spectral region. The experimental frequency dispersions for the five peaks were taken from the fitting procedure applied to the Raman features in Fig. 9(a) and are here plotted together with the theoretical phonon dispersions for monolayer graphene adapted from Popov and Lambin [43] (Fig. 9(b)). The symbols correspond to the frequencies of peaks 1–5 for each laser energy E_L along the high symmetry $K\Gamma$ and KM directions. Squares, circles, triangles, diamonds and stars denote peaks 1–5, respectively. The full lines are the theoretical phonon branches [43] for the combination modes LO+iTA (black), iTO+LA (red), LO+LA (blue), oTO+iTO

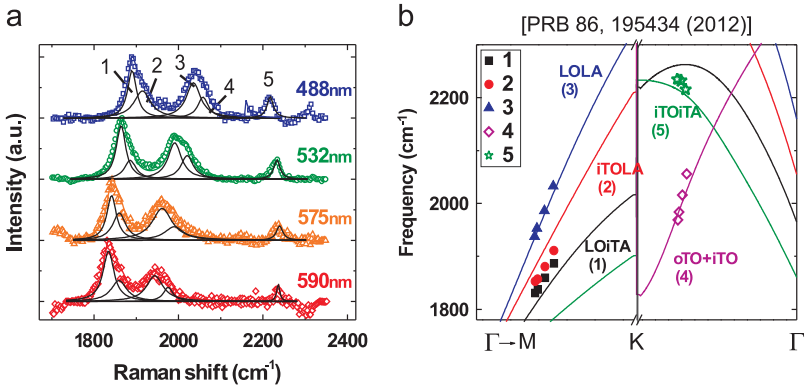

Fig. 9. (Color online) (a) The Raman spectra for the combination modes in the frequency region from 1700 to 2300 cm^{-1} for four different laser lines: 488 nm (2.54 eV), 532 nm (2.33 eV), 575 nm (2.16 eV) and 590 nm (2.10 eV), (b) phonon dispersion of 1LG (solid lines) adapted from Popov and Lambin [43] showing the phonon branch combinations LO+iTA (black), iTO+LA (red), LO+LA (blue), oTO+iTO (purple), oTO+LO (grey) and iTO+iTA (green) near the Γ and the K point. The phonon assignments proposed by Mafra et al. [44] are given by squares, triangles, diamonds and stars correspondingly to peaks from 1 to 5, respectively. The peaks 1, 2 and 3 come from an intravalley DRR process, while the peaks 4 and 5 come from an intervalley DRR process [44].

(purple), oTO+LO (grey) and iTO+iTA (green). The peak numbers given in Fig. 9(a) are written below the corresponding phonon branch assigned to each combination mode. When the peaks can be fitted to a phonon dispersion for either direction of $K\Gamma$ or KM, we can then clearly assign the peak to the corresponding combination mode.

The assignments proposed here are based on and supported by phonon self-energy renormalization calculations and by angle dependent el-ph scattering matrix element calculations, that provide more precise information that was not considered in the previous works [45,46]. These angle dependent scattering calculations give us the direction along which the scattering processes have the highest probability of happening (see the brightest spots in the calculated Fig. 10(d)–(f), where θ_i and θ_f are, respectively, the initial and final scattering angles at the K point measured from the k_x axis). From Fig. 9(b), we can see that the experimental peak 2 (red circles) is in better agreement with the combination phonon branch iTO+LA around the Γ point. Also, as shown in Fig. 9(b), by comparing the experimental and the theoretical phonon dispersions, we can see that peak 3 matches more accurately the phonon branch LO+LA around the Γ point, while peak 4 is in good agreement with the intervalley DRR process around the K point involving the oTO+iTO phonons.

As discussed above, peaks 4 and 5 were assigned by Mafra et al. [44] as, respectively, the oTO+iTO and iTO+iTA $q=2k$ combination modes around the K point generated by an intervalley process. However, the phonon wavevector which is mainly involved in the DRR process lies along either the KM or the $K\Gamma$ directions (considering the high symmetry directions, for simplicity) measured from the K point [48,49] (see Fig. 10(a) and (b) for the distinction between a $K\Gamma$ and a KM process). Fig. 10(c) shows the experimental phonon dispersion for peaks 4 and 5 considering both the KM and $K\Gamma$ directions. The main distinction from the results found in the literature [44–46] lays in the choice of the oTO+iTO or oTO+LO combination modes.

Fig. 10(c) shows that for peak 4 assigned here as the oTO+iTO combination mode, the agreement between the experimental data and the theoretical phonon dispersion points indicates that phonon scattering processes are happening in the $K\Gamma$ direction. However, note that it is delicate to decide whether it is the oTO+LO or the oTO+iTO combination mode that is the correct assignment for this phonon mode, since the frequencies of these combination modes and their dispersions are very close to each other. To make a correct assignment, we used the fact that the directions of the maximum el-ph matrix elements, as well as their phonon self-energy corrections, were as given by varying E_F different for oTO+LO and oTO+iTO (as shown later in the text). Fig. 10(d)–(f) shows the absolute values for the angular dependence of the intervalley el-ph matrix elements for the oTO+iTO, iTO+iTA and oTO+LO phonon combination modes for $E_L = 2.54$ eV, where θ_i and θ_f are, respectively, the initial and final scattering angles defined at the K and K' points. The diagrams in Fig. 10(d)–(f) show the scattering directions for which the el-ph matrix elements are maximum (brightest spots in the figures) for the corresponding combination mode. Looking at the el-ph matrix elements for the oTO+iTO combination mode in Fig. 10(d), one can see that the direction for which the el-ph matrix elements are maximum is closer to the $K\Gamma$ direction. On the other hand, if we look at the scattering diagram for the oTO+LO combination mode in Fig. 10(f), the el-ph matrix elements are a maximum closer to the KM direction. From Fig. 10(c), we can see a better agreement of peak 4 along $K\Gamma$ than along the KM direction.

The experimental data for peak 5 (Fig. 10(c)) is seen to be close to the theoretical curve for both the $K\Gamma$ and KM directions and we must use other information to decide the direction for which the main contribution to the Raman scattering occurs. In Fig. 10(e), we can see that the direction for which the iTO+iTA combination mode has a maximum is closer to the KM direction, from which we conclude that the main contribution to peak 5 comes from an intervalley DRR process in the KM direction. These assignments are confirmed by gate-modulated Raman measurement [44].

Next we discuss the phonon self-energies and the el-ph coupling for those combination modes which were also explored [44]. Fig. 11(a)–(e), respectively, shows the experimental data for the dependence of the phonon frequency ω_q (black solid triangles) and the phonon decay width γ_q (open dots) on V_g (or on the Fermi energy) for the five combination modes.

In Fig. 11(a)–(e), it is seen that ω_q is softened for all the five Raman combination features from 1700 to 2300 cm^{-1}, and that the ω_q softening is accompanied by a broadening of γ_q with increasing carrier concentration (increasing $|V_g|$). This behavior observed for all five combination modes in Ref. [44] is common to Raman modes that come from an AV or EV DRR process with $q=2k$ and is opposite to the behavior observed for the Γ point $q=0$ phonons [38].

The results for phonon self-energy corrections (Fig. 11(a)–(e)) confirm that the Raman combination modes come from a DRR process with $q=2k$ phonons and we also can see that the ω_q and γ_q renormalizations due to the change in the Fermi level position are weak for peaks 1 (Fig. 11(a)) and 3 (Fig. 11(c)), when compared to the other three peaks. In accordance with the assignments given to the peaks and since both of these peaks involve the LO phonon branch, we can conclude that the coupling of this phonon to all the other relevant phonon modes is smaller than compared to peaks 2, 4, and 5. Moreover, the LO mode is not expected to show a strong el-ph coupling when **q** moves away from the Γ point (the LO mode shows a strong coupling only for $q=0$ at the Γ point) [50], which

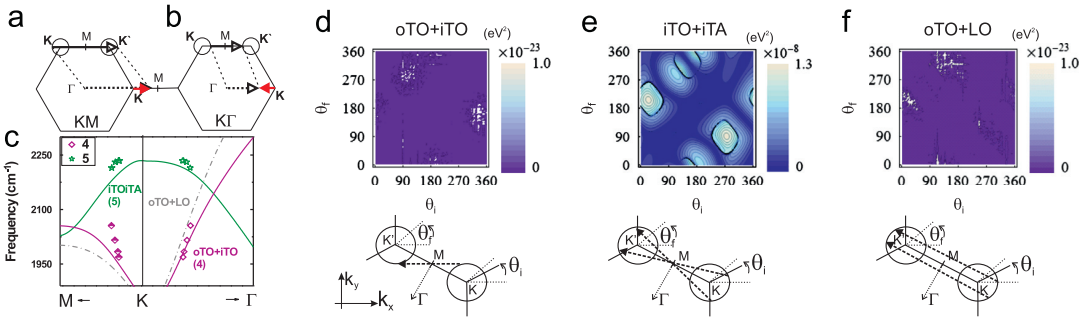

Fig. 10. (Color online) DRR processes involving phonons in the (a) KM or in the (b) $K\Gamma$ direction, respectively, measured from the K point (red full arrows), (c) the phonon dispersion relation for the two intervalley combination modes: peaks 4 (purple diamonds) and 5 (green stars)) combination modes. The half colored symbols correspond to the DRR process in the KM direction and the open symbols correspond to the DRR process in the $K\Gamma$ direction. The absolute value for the angular dependence of the intervalley el-ph scattering matrix elements for the (d) oTO+iTO, (e) iTO+iTA and (f) oTO+LO phonon combination modes for $E_L = 2.54$ eV. θ_i and θ_f are, respectively, the initial and final scattering angles. The diagrams in (d), (e) and (f) show the scattering directions along which the el-ph matrix elements are maximum [44].

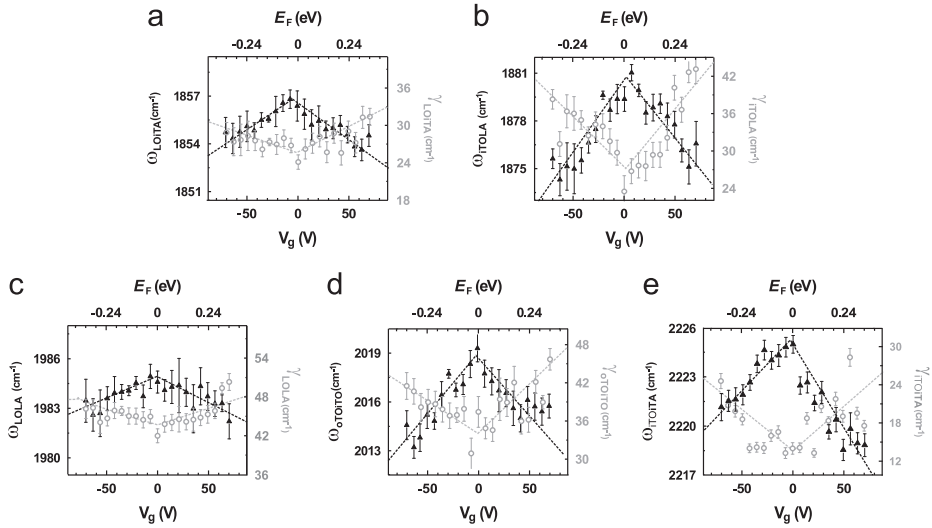

Fig. 11. The dependence of the phonon frequency ω_q (black solid triangles) and phonon decay width γ_q (open dots) on gate voltage (V_g) for the (a) 1, (b) 2, (c) 3, (d) 4 and (e) 5 combination modes in Fig. 9. All the graphics, except for the G band, are on the same scale for better comparisons between the five combination modes. Notice that all five combination modes show a decrease of the ω_q and a broadening of the γ_q with increasing V_g. The dashed lines are guides for the eyes and the error bars come from the fitting procedure [44].

confirms the reason for the assignments to peaks 1 (LO+iTA) and 3 (LO+LA). Since the magnitudes for the self energy correction of peaks 1 and 3 are similar to each other, we conclude that the acoustic modes have zero (small) energy at (around) the Γ point so that they make a negligible contribution to the phonon renormalizations which come from the iTA and LA acoustic modes.

The behavior observed for peaks 4 (oTO+iTO) and 5 (iTO+iTA) is due to the strong el-ph coupling of the iTO phonon branch that is expected at the K point in 1LG. Another interesting observation is that peak 2 (iTO+LA), which is identified with a $q\neq0$ mode around the Γ point, shows that the renormalizations due to the iTO mode become strong when moving away from the Γ point. This is fully consistent with what was observed for peaks 1 and 3 around the Γ point. While the LO mode renormalization weakens, the iTO mode renormalization is strengthened in moving away from the Γ point. The observed gate-dependent behavior consistently confirms the assignments given to the combination modes by Mafra et al. [44], showing that the gate-modulated Raman scattering is indeed a powerful technique to confirm the phonon mode assignments attributed to two Raman peaks which are close in frequency when the V_G and E_L dependencies are both measured and correlated with one another. Note that as regards peak 4, the gate-modulated results are important to decide which is the correct combination mode assignment for this peak, since this peak could have also been assigned to the oTO+LO phonon combination mode, as stated earlier [45]. However, if this assignment were correct, the el-ph coupling would be expected to be similar to what is seen in Fig. 11(a) and (c), which are mode combinations that contain the LO phonon mode. Note that the oTO mode is not expected to show a strong el-ph coupling [50].

5. Electronic Raman spectra and their gate dependence

One of the problems in the Raman spectroscopy of graphene and SWNTs that is not yet well solved is the origin of the Breit–Wigner–Fano (BWF) spectra discussed below. In the presence of free electrons in doped-graphite, doped-graphene or metallic SWNTs, the G band spectra show an asymmetric lineshape with a shifting of the peak position as E_F is changed. This spectral feature shows a BWF lineshape, as was mentioned in the Introduction. In the present section, we provide an overview of our recent measurement of the electronic Raman spectra (ERS) of metallic SWNTs (m-SWNTs) which show a BWF spectral lineshape. The ERS is also sensitively investigated by the gate modulated Raman technique.

When we consider an asymmetric Raman spectrum, we need to consider the continuum spectra, so that we can study the interference effects between a continuum spectrum and a discrete phonon spectrum which is known as the Fano effect [23]. When the constructive (or destructive) interference effect appears at either a lower or higher energy region than the phonon energy, the observed spectra show an asymmetric shape which is described by the BWF line shape (Eq. (9)) as discussed in Section 4. If the constructive interference effect appears at both lower and higher energy regions than the phonon energy, the spectra thus obtained show a symmetric (Lorentzian) lineshape but the intensity is enhanced by the interference effect. The Fano effect appears in many physics situations when: (1) both a continuum and discrete spectra exist over the same energy range, (2) two different optical processes exist with the same initial and final states (coherent processes), and (3) the sign of the interaction changes at the discrete energy level. The interaction between the discrete and continuum spectral features causes the lifetime of the excitation of the discrete level to become finite and thus the discrete spectrum becomes broad. In the case of Raman spectra, the discrete levels are Raman-active phonon modes of zone-centered phonons (a first order process) or double resonance phonons (a second order process). As for the continuum spectra for carbon nanotubes or graphene, we thought in the past that the plasmon was relevant to the inelastic scattering of light, because: (1) the plasmon spectrum becomes continuous from zero energy in low dimensional materials and (2) the BWF lineshape asymmetry is significant only when the Fermi energy is shifted away from the Dirac point by doping.

However, recently, a new broad spectrum has been observed experimentally and identified as the electronic Raman spectrum (ERS) of isolated metallic carbon nanotubes, as shown in Fig. 12 for a (23,14) SWNT [51]. The ERS here appears at 2.08 eV between the RBM and the G band when the energy of the incident laser $E=E_L$ is selected as 2.14 eV. Here 2.08 eV corresponds to the E_{22}^{-} transition energy where the − sign in the superscript of E_{22}^{-} denotes the

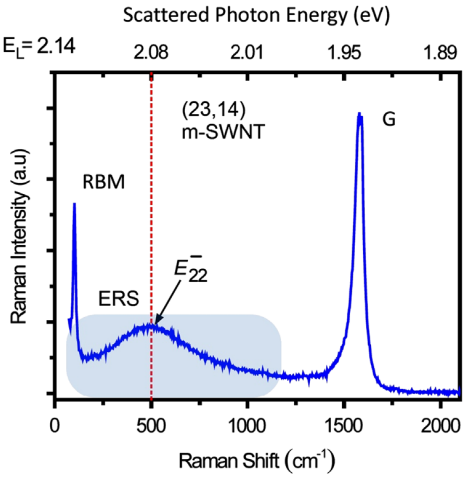

Fig. 12. (Color online) Electronic Raman spectrum (ERS) for the (23,14) metallic SWNT. The ERS spectra appears at 2.08 eV between a RBM and the G band when the energy of the incident laser $E=E_L$ is selected as 2.14 eV. Here 2.08 eV corresponds to the E_{22}^{-} electronic transition energy. The ERS spectra appear only for m-SWNTs [51].

lower energy of the E_{22} transition that is split by the trigonal warping effect [52]. The full width at half maximum intensity (FWHM) of the broad spectral line is around 60 meV ($=484\ cm^{-1}$) which is much broader than the FWHM of the normal phonon feature observed in Raman spectra ($=10\ cm^{-1}$). The ERS is not related to any phonon Raman spectra because: (1) the peak energy position of the ERS does not change by changing E_L, (2) the spectral width of the ERS is much larger than the spectral width of the phonon, and (3) the ERS appears only for m-SWNTs and not for s-SWNTs.

The ERS corresponds to a faster (~10 fs) inelastic scattering process than the scattering by emitting a phonon (~100 fs) whereby an exciton makes a transition from $E=E_L$ (this state is generally a virtual state) to E_{ii} by exciting another exciton in the metallic energy band. The interaction between the two excitons is an electron–electron interaction. Since the exciton in the metallic energy band can be generated for any energy value, the relaxation from $E=E_L$ to E_{ii} is possible for any value of E_L. We can observe this ERS process by probing the scattered light at E_{ii}. Since a typical time for the electron–electron interaction is 10 fs, it is consistent with the fact that the spectral width of the ERS is on the order of $100\ cm^{-1}$. In the case of a metallic SWNT, the exciton in the metallic energy band can not be excited by a photon because the transition is optically forbidden for an electric dipole interaction [53]. On the other hand, an exciton in a metallic energy band can also be generated by a phonon and this results in the Kohn anomaly effect. However, in the case of the Kohn anomaly effect, broad Lorentzian Raman spectra are observed at the phonon energy, which can be clearly distinguished from ERS.

Important evidence that an exciton can be formed in a metallic energy band is that the electronic Raman signal disappears by changing the Fermi energy and this can be directly checked by gate modulated Raman spectroscopy [51]. It should be mentioned that carrier relaxation from a laser excited state $E=E_L$ to a Van Hove singular transition energy E_{ii} is also possible by emitting a phonon (for example a G band phonon) if the energy difference of E_L-E_{ii} is matched to the energy of a G band phonon, which is generally called the scattered resonance Raman spectra. In this case, the Raman spectra that would be observed appear for both m- and s-SWNTs, and have a much narrower spectral width than ERS and we generally see a large enhancement of the Raman intensity compared with the non-resonance case.

When we now select $E=E_L$ so that the phonon G band spectra appear close to the electronic Raman spectral region, then we can see two Raman effects which occur at almost the same frequency so that their line widths overlap with each other, giving both a G band that is broad and a G band with an enhanced intensity. We can see that the asymmetry factor $1/q_{BWF}$ of the G band is changed by observing the shifts in the peak position of the ERS relative to the G band as shown in Fig. 13. In Fig. 13 (right), we see that the value of q_{BWF} decreases (and the G-band becomes more asymmetric) with increasing E_L except for $E_L=2.33$ eV. In the case of $E_L=2.33$ eV, since the difference E_L-E_{ii} is close to the phonon energy, the ERS peaks become weak and the Kohn anomaly effect can be readily seen. The G-band spectra are thus symmetric at $E_L=2.33$ eV and $1/q_{BWF}\sim 0$. The origin of BWF line in a m-SWNT is thus considered to be an interference effect between the phonon mode and the ERS in the presence of the Kohn anomaly effect. Phenomena similar to that shown in Fig. 13 can be observed in graphene, too. Further theoretical study on this topic is now ongoing.

Recently a Raman enhancement effect has also been observed in other phonon spectra when a nanocarbon-based sample of nanotubes or of selected molecules are placed on graphene [54]. The surface enhancement of the Raman signal of a molecule on graphene is called graphene enhanced Raman spectroscopy

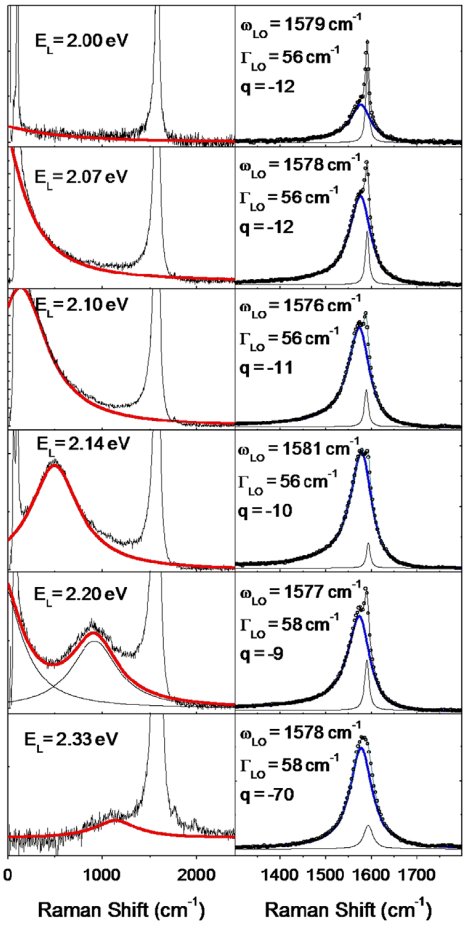

Fig. 13. (Color online) ERS spectra (left) and G-band spectra (right) of a SWNT with different laser excitation energies with E_L values: 2.00, 2.07, 2.10, 2.14, 2.20, 2.33 eV from the top to the bottom of the figure. Red lines are ERS spectra fitted to Lorentzians. When the ERS position is close to the Raman G band at $1580\ cm^{-1}$, then the spectrum between the ERS and the G band changes the asymmetry factor in the Breit–Wigner–Fano formula q_{RBM} drastically, even though the central peak ω_{LO} and spectral width Γ_{LO} do not change much.

(GERS) [54] and the origin of the enhancement is considered to be of chemical origin in which charge transfer between the molecule and the graphene surfaces occurs. The mechanism of GERS is different from that for electronic Raman scattering, with the Raman signal being affected by charge transfer in the case of GERS and by a Kohn anomaly-related effect for the case of ERS.

Another quantum interference effect observed in gate modulated Raman spectroscopy in graphene is the enhancement of the G band that is observed by changing the Fermi energy E_F for a given laser excitation energy, E_{laser}. Kalbac et al. observed an enhancement of the G-band Raman intensity as a function of the Fermi energy while the G′−band intensity monotonically decreases with increasing electrode potential or $|E_F|$ [55]. When the energy E_{laser} of the laser light was increased, the electrode potential (or $|E_F|$) that gives the G band enhancement was found to shift to a higher energy. On the other hand, however, the G′−band did not show any change in the electrode potential dependence of the intensity by changing E_{laser}. This enhancement effect of the G band is independent of the Kohn anomaly effect because the decreases of the Raman intensity due to the spectral broadening by the Kohn anomaly occur at a much smaller electron potential than that for observing the intensity enhancement. Basko predicted from the calculation that the G band intensity is enhanced when the condition $E_F = E_{laser}/2$ is satisfied because of the Pauli Blocking effect of suppressing some possible Raman processes that contribute to the destructive interference [56]. Chen has reported that the constructive interference between the G band and hot luminescence (HL) spectra appears when the $2|E_F|$ is similar to E_{laser} and that the interference is not observed for the 2D (G′) band [57] which is consistent with the results of Kalbac et al. [55]. In order to get the constructive quantum interference between the scattered photon and the HL photon, the phases of the two photons should similar to each other. The HL intensity strongly depends on the $|E_F|$ values and thus some recombination processes such as optical phonon emission is suppressed. A detailed analysis of the dynamics of photo-excited carriers is needed to understand the phase of the HL spectra, which will be a future work.

6. The Kohn anomaly of bi-layer graphene

Finally, we present our results for interlayer (IL)-related phonon combination modes and overtones as well as their phonon self-energy renormalizations in bilayer graphene (2LG), using both gate-modulated and laser-energy dependent Raman scattering spectroscopy. The IL interaction of 2LG gives two energy bands for the π valence and π^* conduction bands and thus in the double resonance scattering process we get up to four possible phonon **q** vectors. The IL interaction does not result in an effect on the in-plane phonon modes since the calculated change of the LO, LA, iTO and iTA phonon frequencies in going from 1LG to 2LG is less than 1 cm^{-1}. As for the out-of-plane phonon modes (oTA, oTO of 1LG), there is both an in-phase and out-of-phase motion of the two graphene layers with respect to each other, respectively, giving rise to the ZA and ZO′ modes for 2LG coming from the oTA mode and the two almost-degenerate ZO modes from the oTO mode which are shown in Fig. 14(a)–(d) [47]. Among the four phonon modes of 2LG, the zone-centered ZO′ and one ZO phonon modes are Raman active since the volume of the unit cell is changed by this vibration. For general q along the phonon dispersion, as shown in Fig. 14(e), we generally have electron–phonon interaction taking place. These phonons are relevant to low-energy phenomena, such as transport and infrared absorption. It is noted that we used a different notation in [47], but here we adjust the notation used in [47] to be compatible with the many references used in this article.

In Fig. 15(a) we show the phonon combination modes and overtones observed in 2LG in the spectral range 1600–1800 cm^{-1}. The insets show the phonon vibrations schematically and their symmetries (following also P_1, P_2, and P_3 notations) together with their respective E_L−dependent frequency dispersions for the LOZA mode (P1, the combination mode of LO+ZA) and the two LOZO′ modes (P2, LO + ZO′) in the upper box in Fig. 15(a)), and the two 2ZO modes (P3, overtone of ZO) in the lower box in Fig. 15(a)). As regards the dispersion relations and the phonon peak assignments, our findings given for the LOZA and LOZO′ combination modes agree well with those reported by Lui et al. [59]. The LOZA mode (P1 in Fig. 15(a)) comes from a q~$2k$ intravalley phonon scattering process (q~$2k$ AV) showing a frequency dispersion $\partial\omega_{LOZA}/\partial E_L = 26.1$ cm^{-1}/eV. By looking at the feature P2 in Fig. 15 (a), we observe that the LOZO′ mode (q~$2k$ AV process) splits into two peaks, LOZO′(+) and LOZO′(−), whose frequency dispersions are $\partial\omega_{LOZO'(+)}/\partial E_L = 55.1$ cm^{-1}/eV and $\partial\omega_{LOZO'(-)}/\partial E_L = 34.2$ cm^{-1}/eV, respectively. As schematized in Fig. 16(c), the two P2 peaks do not arise from the phonon dispersion, but rather, they come from different resonant **q** vectors of the LOZO′ combination mode with the two electronic energy bands (π_1^* and π_2^*) of 2LG. In other words, the two peaks, LOZO′(+) and LOZO′(−) observed in the Raman spectra, come from the same phonon combination mode LOZO′ but probed at two different **q** points connected with

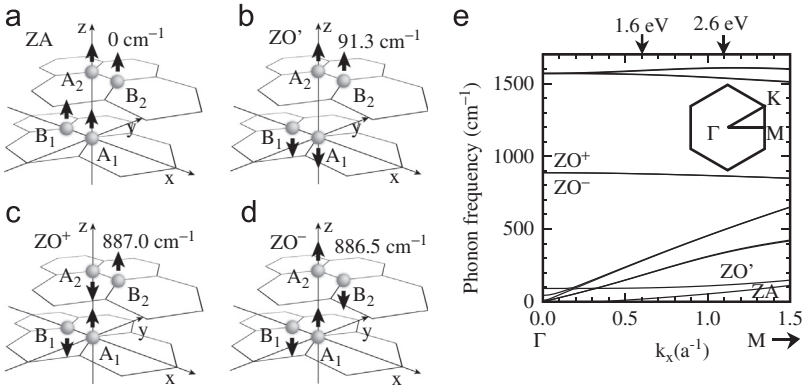

Fig. 14. The lattice vibrations of the four out-of-plane modes for bi-layer graphene (2LG). Here we show (a) the out-of-plane acoustic mode (ZA), (b) the breathing (ZO′) mode, (c) the symmetric mode (ZO^+), (d) the anti-symmetric (ZO^-) tangential optic phonon modes. Two ZO^+ and ZO^- modes are almost degenerate and (e) the phonon dispersion relation of bi-layer graphene along the ΓM line. The resonance points arrows for double resonance Raman scattering are also shown, respectively. $\Gamma M = 2\pi/\sqrt{3}a = 3.63a^{-1}$. Here a=0.246 nm is the lattice constant of two-dimensional graphite. The inset is the Brillouin zone of graphene. It is noted that a different notation is used in [47] but we adjust the notation for other works [58] to be consistent with one another in present article.

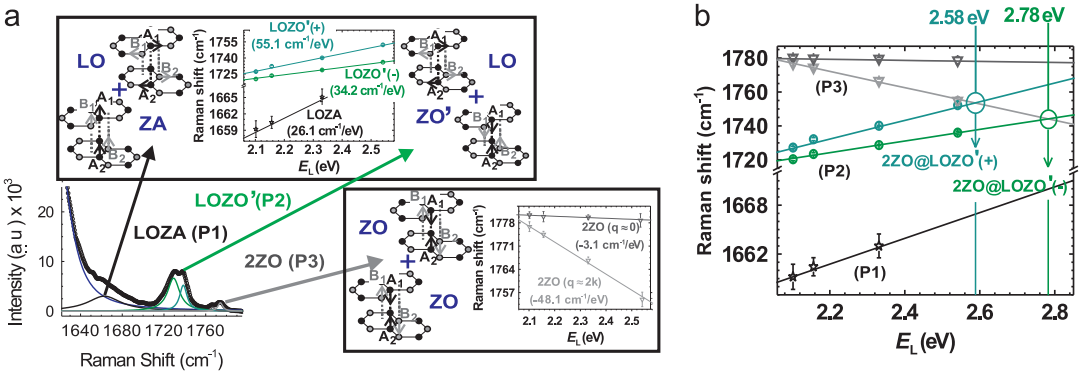

Fig. 15. (Color online) (a) LOZA (P1) and LOZO′ (P2) combination modes and the 2ZO (P3) overtone mode as they appear in the Raman spectra taken with the 532 nm laser line. The solid lines are Lorentzian curves used to fit the spectrum. The upper and lower boxes in (a) show the lattice vibrations associated with each normal mode involved in the combination modes and overtones and their frequency dispersion as a function of E_L, as shown in (b), (b) the Raman shift as a function of E_L, showing that the LOZO′ (P2) combination mode will be crossed by the 2ZO $q \approx 2k$ overtone at 2.58 eV and, according to the dispersion obtained in this work, will likely be crossed again at 2.78 eV. The symbols correspond to the experimental data. The solid lines are the fitting curve results [58].

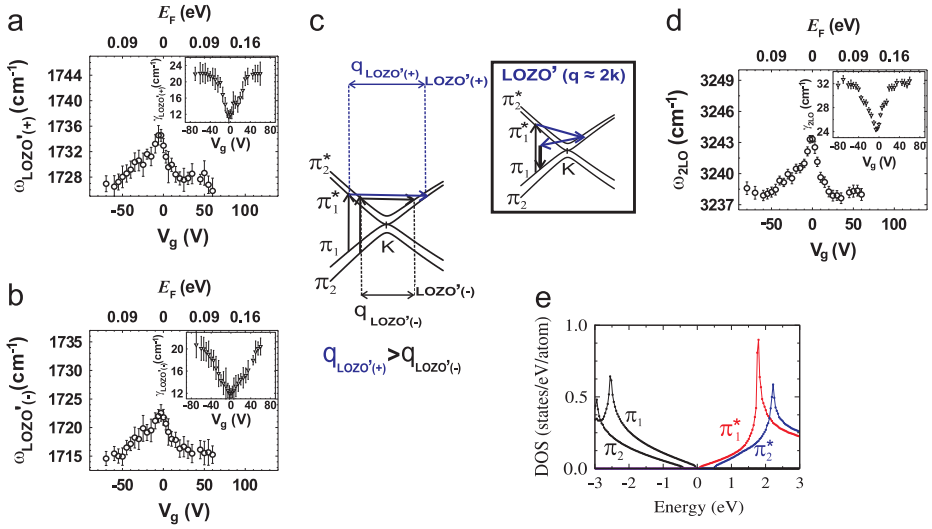

Fig. 16. (Color online) The V_g dependence of (a) $\omega_{LOZO'(+)}$ and (b) $\omega_{LOZO'(-)}$. The insets show the V_g dependence of the linewidth $\gamma_{LOZO'}$, (c) phonon q vectors shown for the LOZO′ combination modes ZO^+ and ZO^- of bilayer graphene 2LG, (d) the V_g dependence of ω_{2LO}. The inset shows the V_g dependence of the linewidth γ_{2LO}, (e) density of electronic states of 2LG for the valence bands π_1 and π_2 (black curves) and for the conduction bands π_1^* (red curve) and π_2^* (blue curve) [58].

LOZO′ phonon dispersion [59]. Actually, the LOZO′(+) corresponds to a resonance process involving the π_1^* band, while the LOZO′(−) corresponds to a resonance process involving the π_2^* band. These resonance conditions (see Fig. 16(c)) require the phonon momentum $\mathbf{q}$ for the LOZO′(+) mode to be larger than that for the LOZO′(−) mode ($q_{LOZO'(+)} > q_{LOZO'(-)}$). As a consequence, the phonon energies are such that $\hbar\omega_{LOZO'(+)} > \hbar\omega_{LOZO'(-)}$ as shown in Fig. 16.

Next, we discuss the two 2ZO (P3) spectra. In 2LG systems (see Fig. 15), the 2ZO overtone should be observed for forward ($q \approx 0$) and backward ($q \sim 2k$) AV scattering, where the $q \sim 2k$ mode shows a negative frequency dispersion [47] (for clarity, in Ref. [47], the abbreviations for the phonon modes are as follows: oTO stands for ZO, M stands for 2ZO, while oTA stands for ZA and ZO stands for ZO′)). While the 2ZO ($q \approx 0$) was discussed by Lui et al. [59], the 2ZO ($q \approx 2k$) remained elusive until later. In 2012, Araujo et al. [58] reported the 2ZO ($q \approx 2k$) mode which was found to show a negative frequency dispersion $\partial\omega_{2ZO(q\approx 2k)}/\partial E_L = -48.1\ \mathrm{cm}^{-1}/\mathrm{eV}$, as seen in Fig. 15(b). As indicated in Fig. 15(b), the 2ZO ($q \approx 2k$) mode crosses the LOZO′(+) at 2.58 eV (also predicted theoretically by Sato et al. [47]). The 2ZO ($q \approx 2k$) mode should have another cross point with the LOZO′(−) mode at 2.78 eV, according to the estimate based on the phonon dispersion [58]. The second crossing at 2.78 eV was not predicted in Ref. [47] but is a consequence of the different dispersions observed for the LOZO′ phonon when this phonon is in resonance with the $\pi_1(\pi_1^*)$ bands or with the $\pi_2(\pi_2^*)$ bands (only the resonance process with the $\pi_1(\pi_1^*)$ bands was considered in Ref. [47]). These phonon mode crossings could affect both the dynamics of the photoexcited carriers and the thermal properties of many systems, since these phonon mode crossings rely on relaxation processes mediated by high-energy optical and acoustic phonons [60,61].

The assignment of the combination modes of 2LG has been sensitively investigated by gate modulated Raman spectroscopy [47]. The Kohn anomaly effect occurs for phonon modes which have electron–phonon interactions such as the ZO, ZO′ and ZA combination modes [34,47,62]. It is noted that the LO mode does not couple with the intralayer interaction and the LO mode does not change with gate voltage in 2LG [58]. As depicted in the inset of Fig. 16(c), the LOZO′ combination mode comes from a $q \sim 2k$ AV process. Note that, Fig. 16(a) and (b) show, respectively, the E_F dependence of $\omega_{LOZO'(+)}$ and $\omega_{LOZO'(-)}$ when V_g is varied. Both, $\omega_{LOZO'(+)}$ and $\omega_{LOZO'(-)}$ soften with increasing $|E_F|$ which is

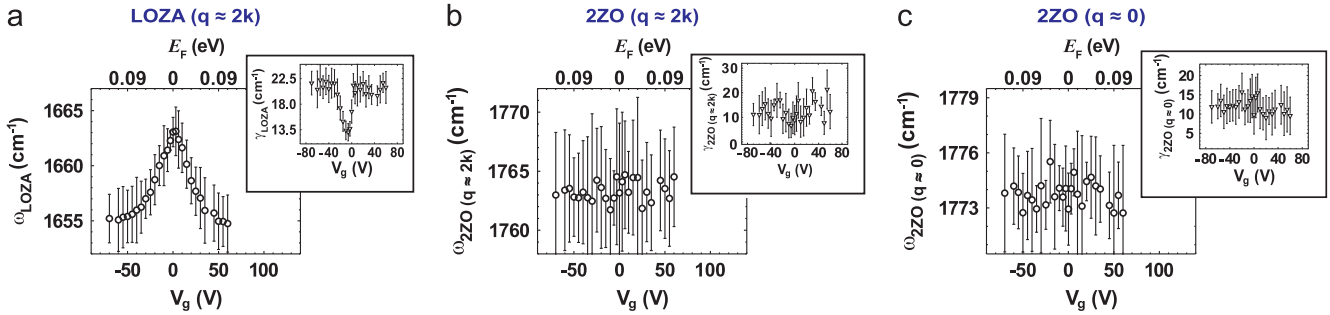

Fig. 17. (Color online) LOZA and 2ZO phonon self-energy renormalizations. (a) and (b) show, respectively, the V_g dependence of ω_{LOZA}, ω_{2ZO} for the $q\approx 2k$ AV process and (c) shows V_g dependence of ω_{2ZO} for the $q\approx 0$ AV process. The insets show the V_g dependence of the line widths γ_{LOZA}, γ_{2ZO} for the $q\approx 2k$ AV process ((a) and (b), respectively) and γ_{2ZO} for the $q\approx 0$ AV process (c).

controlled by increasing $|V_g|$. Correspondingly, as shown in the insets of Fig. 16(a) and (b), the phonon line widths $\gamma_{LOZO'(+)}$ and $\gamma_{LOZO'(-)}$ broaden with increasing $|E_F|$. Analogously, Fig. 17(a) shows that ω_{LOZA} (γ_{LOZA}) softens (broadens) with increasing $|E_F|$, while for the 2ZO overtone, almost no dependence on V_g is observed for both ω_{2ZO} and γ_{2ZO} in Fig. 17(c).

As discussed in Section 4, this behavior is opposite to what happens to the $q=0$ phonons at the Γ−point [38], as is the case of the G-band feature, where $\omega_{\mathbf{q}}$ hardens and $\gamma_{\mathbf{q}}$ narrows when $|E_F|$ increases. On the other hand, the behaviors reported in Figs. 16 and 17 agree with what is expected for $q=0$ AV and $q=2k$ AV/EV phonon self-energy renormalizations. In order to quantify the ZO′ phonon self-energy corrections, the V_g dependence of ω_{2LO} and γ_{2LO} for the 2LO overtone at around 3244 cm^{-1} (see Fig. 16(d)) has been measured, which is known as the 2D′ band with the D band occurring at 1608 cm^{-1} [58]. In analogy to the LOZO′ combination mode about the Γ−point, the 2LO overtone is associated with a $q=2k$ AV double resonant process and is a fruitful choice for unraveling the two-phonon self-energy contributions that are merged in the LOZO′ combination mode.

By inspecting Fig. 16(a) and (b), we find that the renormalization corrections are $\Delta\omega_{LOZO'(+)}=9$ cm^{-1} and $\Delta\omega_{LOZO'(-)}=7$ cm^{-1}, respectively. On the other hand, by looking at Fig. 16(d) we see that $\Delta\omega_{2LO}=5$ cm^{-1}, which means that the LO frequency renormalization for this AV process is $\Delta\omega_{LO}\approx 2.5$ cm^{-1}. The self-energy corrections regarding the LO mode will be the same for the LO contribution for both the LOZO′(+) and LOZO′(−) features. Therefore the phonon self-energy correction $\Delta\omega_{ZO'(+)}$ for the ZO′(+) mode will be given by $\Delta\omega_{LOZO'(+)}-\Delta\omega_{LO}=6.5$ cm^{-1} while the phonon self-energy correction $\Delta\omega_{ZO'(-)}$ for the ZO′(−) mode will be given by $\Delta\omega_{LOZO'(-)}-\Delta\omega_{LO}=4.5$ cm^{-1}. From the analysis above, and remembering that, the larger the self-energy corrections $\Delta\omega_{\mathbf{q}}$, the stronger are the e-ph couplings, we deduce that the interlayer e-ph coupling mediating the renormalizations for the ZO′ mode is stronger than the renormalization for the LO mode. It is noteworthy that the self-energy renormalizations for LOZO′(+) and LOZO′(−) are different, even though they involve the same LO phonon. We understand these differences as follows: the phonon self-energy corrections for $q\neq 0$ phonons rely on the density of electron and phonon states [62]. The density of phonons states will be the same because the same phonon is involved. However, as shown in Fig. 16(e), for energies smaller than |2| eV, the density of electronic states for the $\pi_2(\pi_2^*)$ band is always smaller than that for the $\pi_1(\pi_1^*)$ bands. This means that the phonon self-energy corrections are weaker for the ZO′(−) in comparison to that for the ZO′(+) and this result in not due to a different e-ph coupling symmetry, but because the density of electronic states for $\pi_2(\pi_2^*)$ is smaller in comparison to that for $\pi_1(\pi_1^*)$, as seen in Fig. 16(e). By following the same strategy, we could also estimate the phonon self-energy corrections for the ZA mode, whose LOZA combination mode frequency (linewidth) also hardens (broadens) as expected for the $q\neq 0$ AV processes. As shown in Fig. 17(a), $\Delta\omega_{LOZA}=8$ cm^{-1}. Therefore, the ZA mode self-energy corrections $\Delta\omega_{ZA}$ will be given by $\Delta\omega_{LOZA}-\Delta\omega_{LO}=5.5$ cm^{-1}. It is interesting to note that, the renormalization for the ZA mode is similar to the renormalization correction for the ZO′ mode [58].

Finally, we discuss the V_g dependence of the 2ZO overtone for both, the $q\sim 0$ and $q=2k$ AV processes. Interestingly, the results in Fig. 17(b) and (c) show that, for both cases, the phonon self-energy corrections to the phonon frequency $\Delta\omega_{2ZO}$ and to the line width $\Delta\gamma_{2ZO}$, are weak and as a consequence, the ω_{2ZO} and γ_{2ZO} renormalizations show a constant behavior with increasing $|E_F|$. This result is understood as follows: for phonon self-energy corrections, the phonon energies themselves will determine where in the Dirac cones the e–h pair creation (annihilation) will be happening and, therefore, the phonon energies will determine the initial (final) density of the electronic and vibrational states. On top of this, the momentum conservation requirement $\mathbf{q}=\mathbf{k}-\mathbf{k}'$, which is mostly determined by the slopes in the electronic and vibrational dispersion relations, must be obeyed in order to observe a strong coupling. Comparing all the cases, the ZO phonon mode would create (annihilate) an e–h pair at much higher energies ~110 meV and, therefore, at a much higher density of electronic and vibrational states compared to the energies of the ZA (~3.1 meV) and the ZO′ (~11.2 meV) modes. Because phonon renormalizations can be observed for both the ZA and ZO′ modes, the authors of Ref. [58] understand that the reason behind the weak renormalization observed for the ZO mode is due to the lack of a phonon momentum $\mathbf{q}$ such that $\mathbf{q}=\mathbf{k}-\mathbf{k}'$, and this lack prevents any resonant renormalization from happening. This is confirmed by symmetry arguments since the deformation potential mediating the e-ph coupling is related to the ZO mode, which is an anti-symmetric interlayer vibration (as seen in Fig. 15(a)). The deformation potential is expected to allow a coupling between orthogonal electronic states since the ZO vibration breaks the lattice symmetry, which implies $V_{\mathbf{kk}'}=0$ in Eq. (8). Thus, no renormalizations are expected for the 2ZO mode [63].

7. Summary and future outlook

In this article we show how gate modulation makes Raman spectroscopy, which already had been shown to provide a powerful characterization technique for nanocarbons like carbon nanotubes and graphene, even more powerful than had ever been envisaged before. The physical phenomenon hereby discussed involves using a positive or negative back gate voltage or a top gate voltage to control the position of the Fermi level, or equivalently to control the electron or hole doping concentration of the nanocarbon.

Over the years, many features in the Raman spectra of nanocarbons have been identified and studied. Features, such as the G-band and the radial breathing mode, have become widely known to engineers for characterizing nanotubes for their metallicity and (n,m) chirality. Using gate modulation, it is shown in this review article that each feature in the Raman spectra of nanocarbon materials has its own distinguishing characteristics. After reviewing some of the technical aspects of using back gates and top gates in nanocarbon systems, the fundamental aspects of the Kohn anomaly, which governs the electron–phonon interaction in materials generally, is discussed, giving special emphasis to why the Kohn anomaly is so special for nanocarbon materials, and why the linear $E(k)$ dependence and the K and K′ points in the Brillouin zone, which are related by time inversion symmetry and have a vanishing carrier density at zero wave vector, are so special. The article reviews how small changes in the gate voltage can have a profound effect on the electron and hole populations and on the wave vector q at the Fermi level. These physical effects are vividly seen in each in-plane and out-of-plane phonon mode, combination mode, and harmonic. Many-body and renormalization effects on the frequency and lifetime of the various modes are considered and addressed, thereby explaining many detailed wave vector-dependent effects and distinguishing between $q=0$ and $q\neq0$ related effects. It is shown how gate modulation helps to identify each Raman feature with a specific phonon mode and to identify how many features are present in a given Raman spectrum and what symmetries are relevant to each Raman feature. What is special about the present study is the correlated variation of gate voltage and laser excitation energy E_L to observe and interpret each physical Raman process.

In the future the use of gate modulation should be combined with other experimental techniques by studying differences in the Raman spectra observed when the sample is subjected to two different conditions, such as the use of the isotope ^{13}C rather than ^{12}C which should allow one to separate electronic effects from vibrational phonon effects. Other examples could be the differences between electrochemical and gate voltage changes of the Fermi level, the use of magnetic fields to perturb the electronic structure, time-dependent or pulsed perturbations, strain effects, and combination of these different perturbations. Finally the various findings reported here for graphene suggest the study of each of these physical phenomena in other layered materials like MoS_2 and other transition metal dichalcogenides.

Acknowledgments

R.S. and K.S. acknowledge MEXT grant Nos. 20241023, 25286005, and No. 23710118. D.L.M. acknowledges the support from CNPq-Brazil, SM Projetos LTDA and NSF - DMR 10-04147. P.T. A. acknowledges the support from CNPq-Brazil and ONR MURI N00014-09-1-1063. M.S.D. gratefully acknowledges ONR MURI N00014-09-1-1063.

References

[1] R. Saito, M. Hofmann, G. Dresselhaus, A. Jorio, M.S. Dresselhaus, Adv. Phys. 60 (2011) 413.
[2] A. Jorio, M.S. Dresselhaus, R. Saito, G. Dresselhaus, Raman Spectroscopy in Graphene Related Systems, Wiley-VCH Verlag GmbH & Co KGaA, WeinHeim, Germany, 2011.
[3] M.A. Pimenta, G. Dresselhaus, M.S. Dresselhaus, L.G. Cançado, A. Jorio, R. Saito, Phys. Chem. Chem. Phys. 9 (2007) 1276.
[4] A. Jorio, M.A. Pimenta, A.G. Souza Filho, R. Saito, G. Dresselhaus, M. S. Dresselhaus, New J. Phys. 5 (2003) 139.
[5] M.S. Dresselhaus, G. Dresselhaus, R. Saito, A. Jorio, Phys. Rep. 409 (2005) 47.
[6] S.D. Costa, C. Fantini, A. Righi, A. Bachmatiuk, M.H. Rmmeli, R. Saito, M. A. Pimenta, Carbon 49 (2011) 4719.
[7] W. Kohn, Phys. Rev. Lett. 2 (1959) 393.
[8] K. Sasaki, H. Farhat, R. Saito, M.S. Dresselhaus, Physica E 42 (2010) 2005.
[9] D.L. Mafra, P. Gava, L.M. Malard, R.S. Borges, G.G. Silva, J.A. Leon, F. Plentz, F. Mauri, M.A. Pimenta, Carbon 50 (2012) 3435.
[10] M. Kalbac, H. Farhat, J. Kong, P. Janda, L. Kavan, M.S. Dresselhaus, Nano Lett. 11 (2011) 1957.
[11] K.S. Novoselov, A.K. Geim, S.V. Morozov, D. Jiang, M.I. Katsnelson, I. V. Grigorieva, S.V. Dubonos, A.A. Firsov, Science 306 (2004) 666.
[12] P.R. Gray, P.J. Hurst, S.H. Lewis, R.G. Meyer, Analysis and Design of Analog Integrated Circuits, Fifth edition, Wiley, New York, 2009.
[13] N.W. Ashcroft, N.D. Mermin, Solid State Physics, Saunders College Publishing, Fort Worth, 1989.
[14] J. Yan, Raman Spectroscopy of Graphene, Ph. D. thesis, Graduate School of Arts and Sciences, Columbia University, 2009.
[15] A. Das, S. Pisana, B. Chakraborty, S. Piscanec, S.K. Saha, U.V. Waghmare, K. S. Novoselov, H.R. Krishnamurthy, A.K. Geim, A.C. Ferrari, A.K. Sood, Nat. Nanotechnol. 3 (2008) 210.
[16] J.W. Lamb, Int. J. Infrared Millimeter Waves 17 (1996) 1997.
[17] J. Jiang, R. Saito, A. Grüneis, G. Dresselhaus, M.S. Dresselhaus, Chem. Phys. Lett. 392 (2004) 383.
[18] R. Saito, G. Dresselhaus, M.S. Dresselhaus, Physical Properties of Carbon Nanotubes, Imperial College Press, London, 1998.
[19] R. Saito, A. Grüneis, G.G. Samsonidze, V.W. Brar, G. Dresselhaus, M. S. Dresselhaus, A. Jorio, L.G. Cançado, C. Fantini, M.A. Pimenta, A.G. Souza Filho, New J. Phys. 5 (2003) 157.
[20] A. Jorio, A.G. Souza Filho, G. Dresselhaus, M.S. Dresselhaus, A.K. Swan, M. S. Ünlü, B. Goldberg, M.A. Pimenta, J.H. Hafner, C.M. Lieber, R. Saito, Phys. Rev. B 65 (2002) 155412.
[21] M.A. Pimenta, A. Marucci, S. Empedocles, M. Bawendi, E.B. Hanlon, A.M. Rao, P. C. Eklund, R.E. Smalley, G. Dresselhaus, M.S. Dresselhaus, Phys. Rev. B 58 (1998) R16016.
[22] S.D.M. Brown, A. Jorio, P. Corio, M.S. Dresselhaus, G. Dresselhaus, R. Saito, K. Kneipp, Phys. Rev. B 63 (2001) 155414.
[23] U. Fano, Phys. Rev. 124 (1961) 1866.
[24] H. Farhat, H. Son, G.G. Samsonidze, S. Reich, M.S. Dresselhaus, J. Kong, Phys. Rev. Lett. 99 (2007) 145506.
[25] K. Sasaki, R. Saito, G. Dresselhaus, M.S. Dresselhaus, H. Farhat, J. Kong, Phys. Rev. B 77 (2008) 245441.
[26] M. Lazzeri, F. Mauri, Phys. Rev. Lett. 97 (2006) 266407.
[27] J.S. Park, K. Sasaki, R. Saito, W. Izumida, M. Kalbac, H. Farhat, G. Dresselhaus, M. S. Dresselhaus, Phys. Rev. B 80 (2009) 081402.
[28] J. Jiang, R. Saito, G.G. Samsonidze, S.G. Chou, A. Jorio, G. Dresselhaus, M. S. Dresselhaus, Phys. Rev. B 72 (2005) 235408.
[29] H. Farhat, K. Sasaki, M. Kalbac, M. Hofmann, R. Saito, M.S. Dresselhaus, J. Kong, Phys. Rev. Lett. 102 (2009) 126804.
[30] P.C. Eklund, G. Dresselhaus, M.S. Dresselhaus, J.E. Fischer, Phys. Rev. B 16 (1977) 3330.
[31] M.S. Dresselhaus, G. Dresselhaus, Adv. Phys. 30 (1981) 139, see also Adv. Phys. 5 (2002) 1–186.
[32] R. Saito, A. Jorio, A.G. Souza Filho, G. Dresselhaus, M.S. Dresselhaus, M. A. Pimenta, Phys. Rev. Lett. 88 (2002) 027401.
[33] R. Saito, T. Takeya, T. Kimura, G. Dresselhaus, M.S. Dresselhaus, Phys. Rev. B 57 (1998) 4145.
[34] A.H. Castro Neto, F. Guinea, N.M.R. Peres, K.S. Novoselov, A.K. Geim, Rev. Mod. Phys. 81 (2009) 109.
[35] L.M. Malard, D.C. Elias, E.S. Alves, M.A. Pimenta, Phys. Rev. Lett. 101 (2008) 257401.
[36] J. Yan, E.A. Henriksen, P. Kim, A. Pinczuk, Phys. Rev. Lett. 101 (2008) 136804.
[37] J. Yan, Y. Zhang, P. Kim, A. Pinczuk, Phys. Rev. Lett. 98 (2007) 166802.
[38] P.T. Araujo, D.L. Mafra, K. Sato, R. Saito, J. Kong, M.S. Dresselhaus, Phys. Rev. Lett. 109 (2012) 046801.
[39] M. Lazzeri, S. Piscanec, F. Mauri, A.C. Ferrari, J. Robertson, Phys. Rev. B 73 (2006) 155426.
[40] T. Shimada, T. Sugai, C. Fantini, M. Souza, L.G. Cançado, A. Jorio, M.A. Pimenta, R. Saito, A. Grüneis, G. Dresselhaus, M.S. Dresselhaus, Y. Ohno, T. Mizutani, H. Shinohara, Carbon 43 (2005) 1049.
[41] D.L. Mafra, G. Samsonidze, L.M. Malard, D.C. Elias, J.C. Brant, F. Plentz, E. S. Alves, M.A. Pimenta, Phys. Rev. B 76 (2007) 233407.
[42] S. Pisana, M. Lazzeri, C. Casiraghi, K.S. Novoselov, A.K. Geim, A.C. Ferrari, F. Mauri, Nat. Mat. 6 (2007) 198.
[43] N.V. Popov, P. Lambin, Phys. Rev. B 73 (2006) 085407.
[44] D.L. Mafra, J. Kong, K. Sato, R. Saito, M.S. Dresselhaus, P.T. Araujo, Phys. Rev. B 86 (2012) 195434.
[45] R. Rao, R. Podila, R. Tsuchikawa, J. Katoch, D. Tishler, A.M. Rao, M. Ishigami, ACS Nano 5 (2011) 1594.
[46] C. Cong, T. Yu, R. Saito, G. Dresselhaus, M.S. Dresselhaus, ACS Nano 5 (2011) 1600.
[47] K. Sato, J.S. Park, R. Saito, C. Cong, T. Yu, C.H. Lui, T. Heinz, G. Dresselhaus, M. S. Dresselhaus, Phys. Rev. B 84 (2011) 035419.
[48] J. Maultzsch, S. Reich, C. Thomsen, Phys. Rev. B 70 (2004) 155403.
[49] D.L. Mafra, E.A. Moujaes, S.K. Doorn, H. Htoon, R.W. Nunes, M.A. Pimenta, Carbon 49 (2011) 1511.
[50] S. Piscanec, M. Lazzeri, M. Mauri, A.C. Ferrari, J. Robertson, Phys. Rev. Lett. 93 (2004) 185503.
[51] H. Farhat, S. Berciaud, M. Kalbac, R. Saito, T.F. Heinz, M.S. Dresselhaus, J. Kong, Phys. Rev. Lett. 107 (2011) 157401.

[52] R. Saito, G. Dresselhaus, M.S. Dresselhaus, Phys. Rev. B 61 (2000) 2981.
[53] H. Ajiki, T. Ando, Physica B Cond. Matt. 201 (1994) 349.
[54] H. Xu, Y. Chen, W. Xu, H. Zhang, J. Kong, M. Dresselhaus, J. Zhang, Small 7 (2011) 2945.
[55] M. Kalbac, A. Reina-Cecco, H. Farhat, J. Kong, L. Kavan, M.S. Dresselhaus, ACS Nano 4 (2010) 6055.
[56] D.M. Basko, New J. Phys. 11 (2009) 095011.
[57] C.F. Chen, C.H. Park, B.W. Boudouris, J. Horng, B. Geng, C. Girit, A. Zettl, M. F. Crommie, R.A. Segalman, S.G. Louie, F. Wang, Nature 471 (2011) 617.
[58] P.T. Araujo, D.L. Mafra, K. Sato, R. Saito, J. Kong, M.S. Dresselhaus, Sci. Rep. 2 (2012) 1017.
[59] C.H. Lui, L.M. Malard, S. Kim, G. Lantz, F.E. Laverge, R. Saito, T.F. Heinz, Nano Lett. 12 (2012) 5539.
[60] T.J. Echtermeyer, L. Britnell, P.K. Jasnos, A. Lombardo, R.V. Gorbachev, A. N. Grigorenko, A.K. Geim, A.C. Ferrari, K.S. Novoselov, Nat. Comm. 2 (2011) 458.
[61] O. Delaire, J. Ma, K. Marty, A.F. May, M.A. McGuire, .Du M-H, D.J. Singh, A. Podlesnyak, G. Ehlers, M.D. Lumsden, B.C. Sales, Nat. Mat. 10 (2011) 614.
[62] L.M. Malard, J. Nilsson, D.C. Elias, J.C. Brant, F. Plentz, E.S. Alves, A.H. Castro Neto, M.A. Pimenta, Phys. Rev. B 76 (2007) 201401.
[63] B. Chakraborty, A. Bera, D.V.S. Muthu, S. Bhowmick, U.V. Waghmare, A.K. Sood, Phys. Rev. B 85 (2012) 161403. (R).